RANGE-DOPPLER, TARGET-REFERENCING IMAGING SYSTEMS (RD-TRIMS)

M.L. Minden and T.R. O'Meara

Hughes Research Laboratories

3011 Malibu Canyon Road

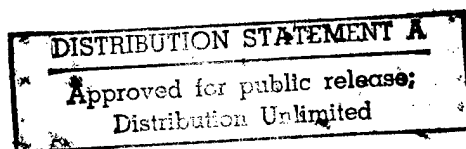Malibu, California 90265

January 1990

N00014-85-C-0534

Final Report

August 1, 1985 through December 31, 1988

19990222054

REPORT DOCUMENTATION PAGE

Form Approved
OMB No. 0704-0188

1a. REPORT SECURITY CLASSIFICATION	1b. RESTRICTIVE MARKINGS
Unclassified	

2a. SECURITY CLASSIFICATION AUTHORITY	3. DISTRIBUTION / AVAILABILITY OF REPORT
	Unlimited
2b. DECLASSIFICATION / DOWNGRADING SCHEDULE	

4. PERFORMING ORGANIZATION REPORT NUMBER(S)	5. MONITORING ORGANIZATION REPORT NUMBER(S)

6a. NAME OF PERFORMING ORGANIZATION	6b. OFFICE SYMBOL (If applicable)	7a. NAME OF MONITORING ORGANIZATION
Hughes Research Laboratories		

6c. ADDRESS (City, State, and ZIP Code)	7b. ADDRESS (City, State, and ZIP Code)
3011 Malibu Canyon Road Malibu, CA 90245	

8a. NAME OF FUNDING / SPONSORING ORGANIZATION	8b. OFFICE SYMBOL (If applicable)	9. PROCUREMENT INSTRUMENT IDENTIFICATION NUMBER
Office of Naval Research	ONR	N00014-85-C-0534

8c. ADDRESS (City, State, and ZIP Code)	10. SOURCE OF FUNDING NUMBERS			
800 N. Quincy Street Arlington, VA 22217	PROGRAM ELEMENT NO.	PROJECT NO.	TASK NO.	WORK UNIT ACCESSION NO.

11. TITLE (Include Security Classification)

RANGE-DOPPLER, TARGET-REFERENCING IMAGING SYSTEMS (RD-TRIMS) (U)

12. PERSONAL AUTHOR(S)
M.L. Minden and T.R. O'Meara

13a. TYPE OF REPORT	13b. TIME COVERED	14. DATE OF REPORT (Year, Month, Day)	15. PAGE COUNT
Final	FROM 8/1/85 TO 12/31/88	1990, January, 18	75

16. SUPPLEMENTARY NOTATION

17. COSATI CODES			18. SUBJECT TERMS (Continue on reverse if necessary and identify by block number)
FIELD	GROUP	SUB-GROUP	Optical range-doppler imaging Target signature extraction
			High resoltion imaging

19. ABSTRACT (Continue on reverse if necessary and identify by block number)

RD-TRIMS (Range-Doppler Target-Referencing, Optical-Imaging Systems) is a new imaging concept that enjoys pulsed, visible laser illumination. It differs from conventional microwave and infrared range-Doppler (RD) imaging radars in that the return wave is self-referenced rather than referenced to a local oscillator. This results in enormously reduced coherence requirements for the source and permits visible Doppler systems to be implemented, with the advantage of increased reflectivity, resolution, and illumination efficiency. In this program, analytic and computer models of an RD-TRIMS system were developed to explore the feasibility of the proposed concept. For the simple models we investigated, excellent images and signature information were obtainable.

20. DISTRIBUTION / AVAILABILITY OF ABSTRACT	21. ABSTRACT SECURITY CLASSIFICATION	
☐ UNCLASSIFIED / UNLIMITED ☒ SAME AS RPT. ☐ DTIC USERS	Unclassified	
22a. NAME OF RESPONSIBLE INDIVIDUAL	22b. TELEPHONE (Include Area Code)	22c. OFFICE SYMBOL

DD Form 1473, JUN 86   *Previous editions are obsolete*   SECURITY CLASSIFICATION OF THIS PAGE

TABLE OF CONTENTS

LIST OF ILLUSTRATIONS

SUMMARY OF RD-TRIMS CONTRACT

RD-TRIMS (Range-Doppler Target-Referencing, Optical-Imaging Systems) is a new Doppler imaging concept that can be used with pulsed, visible laser illumination. It differs from conventional microwave and infrared range-Doppler (RD) imaging radars in that the return wave is self-referenced rather than referenced to a local oscillator. This results in enormously reduced coherence requirements for the source and in elimination of aberration-induced fade out in the beat signal, factors which have made visible Doppler systems difficult to implement in the past. The advantages of operating at visible wavelengths include increased reflectivity, resolution, and illumination efficiency. The self referencing permits the receiver to employ large-area, inexpensive receiver optics without concern for atmospheric propagation or figuring errors. In this program, analytic and computer models of an RD-TRIMS system were developed to explore the feasibility of the proposed concept. For the simple models we investigated, excellent images were obtainable and good speckle reduction was observed.

SECTION 1

INTRODUCTION

This report describes and analyzes a novel active imaging system for operation at optical wavelengths,of the Range Doppler (RD) class. In all RD systems, the image information content is contained in the differential Doppler shift information embedded in the range gated optical radar returns from the various reflecting elements of a target or image object. These Doppler shifts are generated by relative object rotations or vibrations. The resolution of these systems is determined by the range resolution (effective pulsewidth) and the Doppler resolution (integration time) of the system. Thus, if coherence and SNR can be maintained, the available resolution is <u>not</u> impacted by either the range or the λ/D ratio of the receiver aperture. This is a major motivation for considering these systems. Another reason is the unique signature information that these systems may provide.

The systems under consideration here differ from conventional microwave and infrared range-Doppler imaging radars in that they are self-referencing or, more precisely, target referencing. That is, a particular return from the target itself is selected as a frequency reference that beats against all of the other target returns in order to extract their differential Doppler content. Therefore, we call the proposed systems Range-Doppler Target Referencing Imaging Systems (RD-TRIMS).

The advantages of a self-referencing approach are substantial. The most significant is that the illuminator coherence length requirement is greatly reduced. The conventional systems require coherence lengths equal to the round-trip distance from the illumination source to the target. In contrast, the current approach requires coherence lengths that are only a fraction of the target dimension. Additionally,

1

since both the reference and the image information stem from the same source, there is no need for whole-body Doppler acquisition and tracking, as is required in conventional range-Doppler systems. Whole-body Doppler shifts, for objects in low orbits, can amount to more than 10 GHz at visible wavelengths, which presents major tracking problems.

Further, one escapes another class of problem often experienced by the conventional type of RD system, when implemented at optical wavelengths. This problem results from wavefront aberrations introduced on the return beam either by atmospheric propagation or by a badly figured receiver telescope. With large receiver apertures, these aberrations typically destroy the spatial coherence between the focused signal return and the local oscillator beam, at the detector input. This results in a random, time-varying, spatial phase modulation of the detector ac currents, producing a weak and strongly fluctuating signal at the detector output. The common path nature of the proposed system eliminates this turbulence problem, and makes it possible to greatly reduce the receiver telescope figure requirements, thereby reducing system cost.

A conventional RD imaging system is typically implemented as a coherent microwave radar. We will provide a brief review of these systems in Appendix A, by way of background. Although our proposed self-referencing systems have utility at any wavelength, including microwaves, the main discussion will concentrate on optical implementations at visible wavelengths, where the major benefits of the self-referencing approach accrue. Moreover, the relaxation of the coherence length requirement makes visible lasers viable candidates for Doppler imaging. Advantages for operating RD imaging systems at visible wavelengths are reviewed in Appendix B. Briefly, these are:

    (1)   Generally, as the wavelength decreases, more and more of the image object reflecting area effectively participates as an observable backscatterer, so that the information content in the image becomes enhanced.

(2) For a given set of differential velocities the frequency shift and hence, the Doppler resolution is higher at visible wavelengths. Thus signature information can be extracted in a short time, before the image object has substantially reoriented in aspect.

(3) The Doppler sensitivity is much better at visible wavelengths. More precisely, submicron vibrations should produce a substantial phase/frequency modulation signature. Therefore we expect an associated S/N which is quite strong, in comparison to longer wavelength range Doppler systems.

(4) Assuming that only a single object at a known location is to be illuminated, a shorter wavelength, optical-radar illuminator source more efficiently illuminates the object, for a given diameter of illuminator aperture, at the shorter wavelengths.

These benefits appear to be obtainable only at some cost in receiver complexity, if maximum S/N performance is to be achieved. Accordingly, Section 2.0 discusses in more detail how a self-referencing Range Doppler imaging system might be implemented, and discusses the expected S/N performance. Since no visible RD images have ever been recorded to the best of our knowledge, we have elected to present a brief comparison of this class of imaging to angle-angle imaging in Section 3.0 analyzes the expected S/N performance. Section 4.0 discusses the computer modeling results for two simple classes of image object.

3

SECTION 2

SYSTEM IMPLEMENTATIONS

In this section we will discuss the operating principles of an RD-TRIMS system and then discuss some of the technology issues concerning implementation at visible wavelengths. Section 2.1 discusses the basic operating principles of the target-referencing range-Doppler imaging systems. Section 2.2 discusses the PRF requirements, which strongly impact the nature of the required illuminator. Section 2.3 discusses the relative importance of the target reference parameters and how a reference might be selected. Section 2.4 discusses some concepts for implementing high sensitivity receiving systems, as would be desired for long range operation. Section 2.4 presents a S/N analysis for several classes of these receivers. In order to implement these receivers, high-speed optical switches, with good switching efficiency, are required and Section 2.5 discusses how these switches might be developed. Although these systems can be implemented as long pulse ($\sim\mu$sec) pulse compression radars (as in typical microwave imaging radars) this report limits its discussion to short pulse ($\sim$nsec), high PRF system implementations.

2.1 BASIC SYSTEM PRINCIPLES

In common with conventional RD systems, the RD-TRIMS system makes use of range-gated laser pulse reflections from the image object. With RD-TRIMS, however, a repetitive laser pulse train produces returns which are delayed by different amounts from different regions of the target and divided at the receiver into time segments associated with the distance to the reflecting region. One of the range-gated return segments is selected as a frequency reference wave against which the returns from other segments are beat. As the object moves in translation, rotation or vibration, the change in relative phase between the range and

reference segments creates a time-varying, sample data signal. More specifically, the reference signal is spatially separated from the image signals by temporal gating and translated in frequency, to produce a beat in the detector output at an intermediate frequency. This intermediate frequency signal could be processed by a Doppler filter bank of crystal filters. Alternatively, it could be downconverted, digitized and stored as a real number sequence from which the Doppler components can be extracted. The latter approach was employed in our computer simulations. In either case, a Doppler image can then be formed, in which each image point on the object is associated with a particular range bin, selected by the pulse delay time, and a particular velocity bin (or Doppler) component in the source/receiver (line of sight) direction.

A simplified, visible, range-Doppler, self-referencing imaging system is illustrated in Figure 2-1. In this system an object is being illuminated by a high PRF, mode-locked laser. Each illuminator pulse scatters off of the object and produces a train of reflected returns; only two of these [(R_1) and (R_2)] are shown in the figure. The first to return to the receiver (R_1) is assumed to have been reflected from the convex leading edge of the object and is used as the reference. The second returning pulse (R_2) is the reflection from one particular range cell. These two returns are brought into temporal coincidence by spatially separating them, via beam splitters, and then, after their propagation paths are equalized, recombining them via additional beam splitters. The path separation also permits one return (here the reference) to be frequency offset from the other. The two return pulse fields are thus brought into temporal overlap and will coherently interfere, or beat, upon recombination. The composite intensity of this beat is detected (in this example) by a noncoherent detector, while the frequency of the beat is given by the frequency offset plus or minus any differential Doppler shifts which occur between the reference and reflecting element or "image" component.
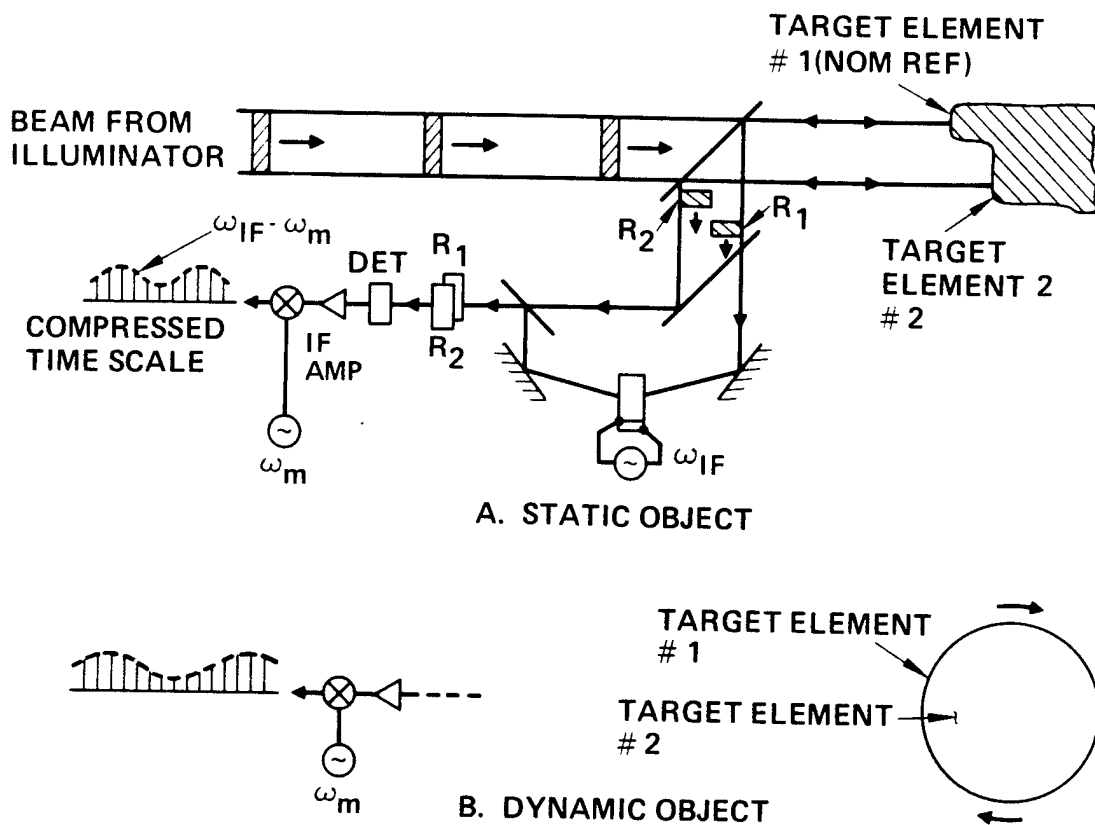
Figure 2-1.   Simplified self-referencing range-Doppler imaging
system.

Since the overall propagation paths of the image cell and the reference cell total are closely matched, the laser need only have a coherence length which is equal to the pulse length in order to achieve a beat between the image and reference components. Thus, the system functions as a coherent radar even though a local oscillator would generally not be incorporated for visible systems (local oscillator system variants have been conceived for use at 10.6 μm). With this approach, one substitutes the reflection (R_1) from a particular image-object reflectivity element for the local oscillator reference of the conventional coherent radar.

The frequency offset between the reference and image pulses establishes the intermediate frequency (IF) and is produced, in the example of Figure 2-1, by passing the reference through an acousto-optic (Bragg-cell) modulator. The IF would normally be chosen to be on the order of one-third the laser PRF or less. Clearly, the highest differential Doppler shift, which occurs across the image object of interest, must be less than the IF, if one is to avoid spectral foldover problems.

Note that each pulse of the optical beat signal into the detector is typically on the order of subnanoseconds in duration, which is far too short to represent any significant portion of the IF, or of the Doppler signal frequency content that perturbs the IF. Thus, if the detector were very fast, its output, as generated by an extended train of return optical pulses (without differential Doppler shift), would be a train of current pulses, whose envelope is sinusoidally modulated at the IF (for no differential Doppler shift), as illustrated in Figure 2-1(a). In most cases it will prove useful to further reduce the IF output for subsequent digital processing by means of a down converter at ω_d.

For static objects, as illustrated in Figure 2-1(a), the envelope associated with the ensemble of the current pulses out of the RD detector is modulated at exactly the Bragg-cell drive

frequency ω_{if}, since each image cell has a zero differential doppler shift with respect to the reference. However, with vibrating or rotating objects, or with objects that have an apparent rotation about the line of sight, the IF is typically offset by one or more differential Doppler shifts as produced by the relative movement between the reference and the image cells. This is illustrated in Figure 2-1(b) for a rotating object. Only one of the shifted frequencies, out of the many which are generated by a rotating object, is illustrated.

For both static and dynamic objects, one employs either a postdetection filter or a low-bandwidth optical detector, and the individual pulses are averaged out, so that only the temporal variations representing the modulation envelope, at or near the IF, are seen at the detector output. These variations are illustrated by the dashed lines in Figures 2-1(a) and (b).

In the simplified system of Figure 2-1(a), one particular delay line setting is employed to bring the arriving signals from one particular range bin into temporal coincidence with the reference signal pulse at the detector. Signals arriving at the detector from other range bin elements are not in temporal coincidence with the reference and produce no detector output near the IF signal in frequency, and thus the amplifier IF filters eliminate such components.

The delay line must be sequentially reset in optical path length in order to sample each of the other range bins for their Doppler signal content. In practice, both the reference and the image cell return signals are split out from the ensemble of the returning signals by high-speed optical range gates (which are not illustrated in Figure 2-1, but which will be discussed subsequently).

We will name a system, of the type illustrated in Figure 2-1(a), as a heterodyne self-referencing (or target referencing) system, since a deliberate frequency offset is introduced between the reference and imaging paths. Homodyne

self-referencing approaches are also possible and may be appropriate for those imaging problems where range ambiguities do not permit the high PRFs required to implement a heterodyne system.

Although we believe the major utility of the self-referencing approach is in the implementation of visible optical radars, the same concepts can clearly be implemented at 10.6 μm wavelengths, at millimeter wavelengths, or at microwave wavelengths with many of the same potential benefits. At these longer wavelengths it will be advantageous, from a detector sensitivity viewpoint, to employ one or more detectors operating with a common local oscillator. One approach (which would employ a single conventional heterodyne detector) is to separate the reference and the various range-bin pulses by high-speed electronic switching of the IF signals out of the detector. The electronic signal pulses would be brought into temporal coincidence, using electronic or surface wave delay lines, and electronically beat against each other. Another approach is to use multiple detectors, with each detector servicing one range bin. The required time gating (to select the correct return pulse) could be achieved via short pulse time gating of the local oscillator. Although these approaches require a Doppler-tracking local oscillator, the requirement for long coherence length transmitters and local oscillators is still avoided.

The nature of the IF signal will be discussed next. This IF signal has a frequency distribution that centers on the nominal IF introduced by the Bragg cell, with plus or minus deviations corresponding to the range of differential Doppler offsets, produced by all of the target reflectivity cells which fall within the selected range bin. The selected (center) IF must be closely related to the illuminator and its choice, in turn, is strongly impacted by the number and distribution, in range and angle, of the objects to be imaged.

The remainder of the section discusses key technology issues involved in the synthesis of such imaging systems, and the nature of the references which we expect to employ.

2.2   CHOICE OF ILLUMINATOR PRF AND FREQUENCY OFFSET

The choice of laser illuminator and PRF is dependent on the size, distribution, and number of objects. For the case of single objects within the illuminator field-of-view (FOV), the upper bound on the PRF is set by the requirement to spatially separate the pulses of the illuminator pulse train by a sufficient distance to avoid single-object range ambiguities in the return signal. The separation should be greater than twice the depth of the object to ensure that the object returns from one illuminator pulse do not overlap with returns from the next illuminator pulse arriving from a different portion of the target. In radar terminology, this is called "unambiguous ranging." For the imaging of isolated objects, this requirement is not difficult to meet and one might employ a high-average-power mode-locked visible laser, operating either quasi-cw or in a pulse burst mode, with a PRF somewhere in the vicinity of 20 to 40 MHz. If we choose 30 Mhz, for example, one can avoid range ambiguities for objects less than 16 ft. in depth.

Since the TRIMS systems discussed in this report operate on a sample-data basis, they must incorporate an illuminator with a PRF sufficiently high to sample the IF signal frequency, with a minimum rate of three samples per cycle. For low-pass signals the Nyquist criterion is two samples per period where the period corresponds to the highest frequency. The band-pass case is more demanding. For the 30 Mhz laser PRF, the lower bound on the intermediate frequency is 10 Mhz. Thus, if a Bragg cell is employed it must operate at 10 Mhz to produce this intermediate frequency. It is also necessary to produce an IF frequency which is sufficiently large to avoid spectral fold-overs. This requirement typically would set the lower bound on the illuminator PRF.

However, if several objects fall within the illuminator FOV, then one must also ensure that the returns from one illuminator pulse, illuminating any object, do not temporally overlap with returns from other illuminator pulses, illuminating any other object within the FOV. This is a more challenging problem, since the positions of the objects may not be known in advance. This class of object range distribution requires that more complex pulse burst trains be employed. It should be noted that the narrow beam illuminators (typically of the order of 10 μrad with atmospheric paths) which are achievable with visible illuminators, greatly reduces the probability of range ambiguity problems for multiple objects.

One other consideration could impact the choice of PRF. For visible imaging radars which must image against a cloud background, radar reflection from the clouds can generate a strong shot noise component in the detector output. The predetection optical range gating employed in our example systems, operating in conjunction with pulse burst operation, can eliminate this problem.

2.3 CHOOSING A REFERENCE

In RD-TRIMS systems, a range-gated return signal from an image object reflectivity element is selected as the reference. The reference effectively functions as a surrogate "local oscillator" and requires one attribute for best quality imaging. The object area selected by the range gate must contain substantially only one Doppler frequency. More specifically, the variation in radial velocity across the scattering centers, encompassed within the reference range bin, must be small compared to the significant variations that occur between two adjacent object scattering centers.

It is helpful, in enhancing the S/N performance, if this reference is bright (10 to 100 times a single range Doppler cell intensity), but there is no requirement for strong references

from an imaging viewpoint, for reasons discussed below.
Furthermore, the reference need not maintain the polarization of
the illuminator.

Two basic classes of reference are illustrated in
Figure 2-2. Most likely the reference that would be selected is
the closest leading edge of a convex surface, as illustrated in
Figure 2-2(a). The reference element could, in principle, be a
diffuse Lambertian scatterer. With most paints and surfaces,
one typically sees a weak specular component as well, which will
improve S/N performance. Thus, although a specular component is
not essential, it can be helpful. Further, it is expected that
sometimes a single bright glint can be found within a single
range cell, which can also be selected for referencing by an
appropriate range gating [Figure 2-2(b)]. Again, this will
enhance S/N. It is important that the secondary glints be
eliminated by the range gate since these will produce multiple,
overlapping, displaced images.

2.4 HIGH SENSITIVITY RECEIVERS

The RD-TRIMS system of Figure 2-3 is intended to serve as a
conceptual tool, or possibly as a prototype for laboratory
demonstration. However, it is not very photon-efficient since,
while the image range-cell delay line is processing a particular
range bin, the photons which are arriving from other range bins
are being lost. Still worse, they generate excess shot noise
rather than useful image information. We have conceived of
several more efficient methods of simultaneously processing the
return signals from all range cells, resulting in much higher
S/N performance. We next discuss two of these, which differ in
the number of detectors and in the manner of encoding the return
information into the detectors. Both approaches require high-
speed optical switches, which rapidly sequence the returning
pulses through a series of fixed, optical delay lines. These
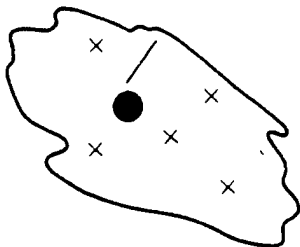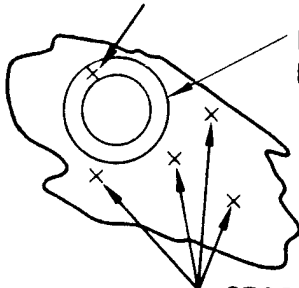switches, as well as the optical delay lines, have several

TYPE OF REFERENCE   ADVANTAGE

REFERENCING FROM THE LEADING EDGE RETURN

                                     ALWAYS
                                     AVAILABLE

RANGE-GATED GLINT   REF GLINT

                                     ENHANCED
                                     S/N PERFORMANCE

SECONDARY GLiNTS

Figure 2-2.   Two basic classes of references which can be
               selected by range gating.

implementation approaches. In all cases the signals are separated into reference and image components according to return range bins (or time of arrival).

One of the enhanced receivers, which employs multiple detectors, is illustrated in Figure 2-3. In this system, a separate detector is used to process the returns from each range bin as they arrive at the receiver. The reference pulses are selected by time gating, are frequency shifted, and are delayed and split into many paths that service the multiple detectors, one per range bin. The various image element returns are similarly selected out from the composite return by optical time gating. The image pulses from increasingly distant object elements arrive at the receiver in temporal progression, and each pulse is split out of the main optical path by very-high-speed EO switches S1, S2, S3 (which are activated in synchronism with the pulse arrival) and polarization sensitive beam splitters. The high-speed switches could possibly be of the "mode-locked" variety (see Section 6 below). The split-out pulses are then delayed by appropriate optical delay lines and brought into spatial overlap with the reference pulse via recombining beam splitters. The delay lines ensure that each signal pulse combines in temporal synchronism with the reference pulse at each range bin detector. Thus, in effect, each range-bin selected set of image cells is serviced by an (almost) balanced-path, Mach-Zender interferometer, which includes the round-trip paths to the various object range elements.

Clearly the beam combining of the reference and signal beams must be done with care, both to be efficient and to avoid cross coupling from one range bin signal into another. If there is a polarization separability between the reference and image cell returns, then the splitting system can be designed to exploit it, as discussed under the referencing section above; however, we do not count on it. For this reason we have included a rather unusual 45° oriented, polarization sensitive
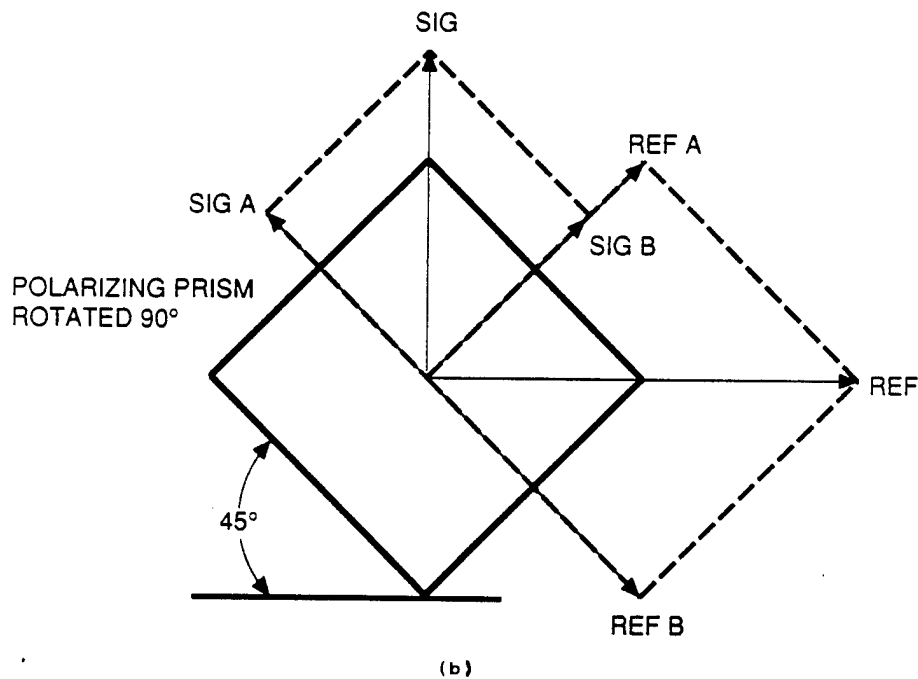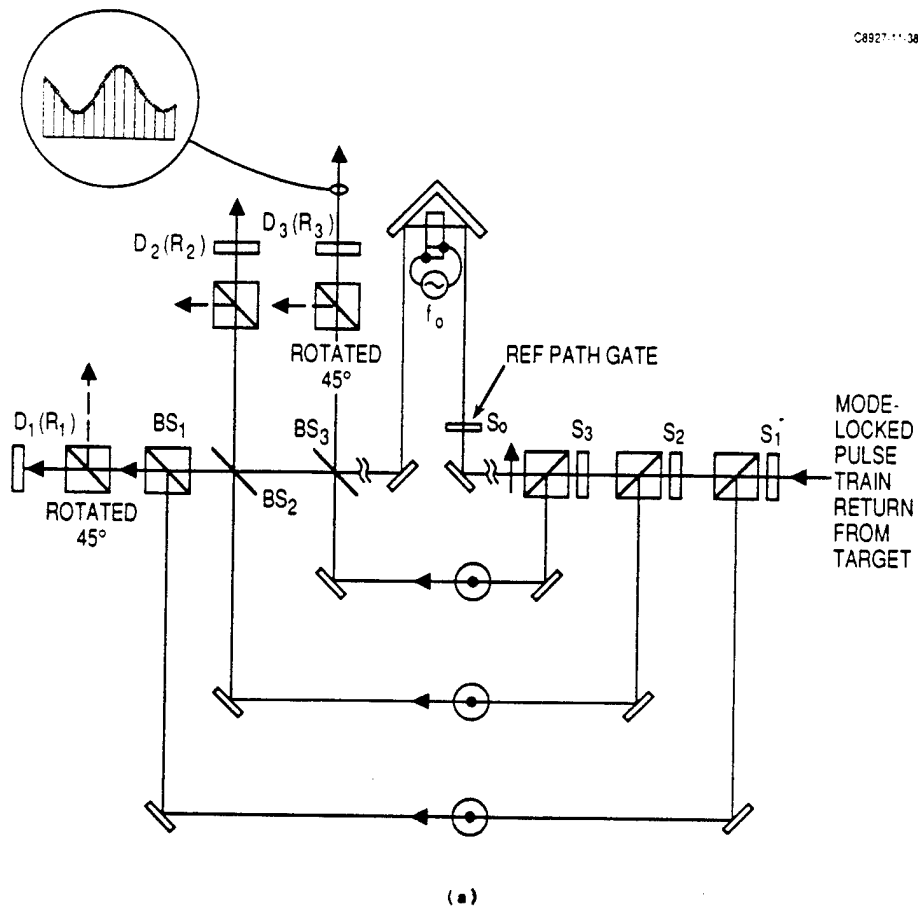
C8927-11-38

C8927-11-41R

(a)

(b)

Figure 2-3.   A multiple-detector implementation of a high
sensitivity RD TRIMS receiver.

15

beam splitters (e.g., Glan-Thompson) for recombining and interfering the beams. Specifically, the image and reference pulses are rotated in polarization by 45° relative to the normal pass (or reflection) orientations as illustrated in Figure 2-5b. Each signal and reference field may be decomposed into A and B components at 45° to the original, one of which is passed by the polarizer while the other is reflected. The reference and imaging pulses exiting the polarizer are thus copolarized and can intefere at detectors servicing either output. Thus, a second set of copolarized beams reflects off of the GT splitter, as shown by the dashed lines may be used to drive a second set of detectors (not illustrated in Figure 2-3), whose output is a 180°-phase-shifted replica of the illustrated signal. Both detector output signals can be coherently combined, via an electronic inverter, to produce an enhanced S/N.

It is possible to devise systems which require only a single detector and IF amplifier, and which avoid the requirement to split the reference power into parallel paths, as illustrated in Figure 2-4 by employing a distinctive frequency encoding on each range-cell signal return. In this system variant, each range-bin return pulse is frequency tagged and appropriately delayed. These frequency shifters could be EO devices yielding a small up or down conversion or by one or more Bragg cells. The outputs are then combined with the reference, in temporal coincidence and in angular registration, by means of a second Bragg cell and polarizing 45° oriented beam splitter and of the combined signals could, in principle, illuminate a single detector whose output services all range bins simultaneously. The detector outputs are then separated into the discrete range bins by multiple IF filters centered on each encoded IF frequency band. Note that the best S/N performance is obtained, as in the multiple detector systems, by using the balanced detector system illustrated in Figure 2-4.
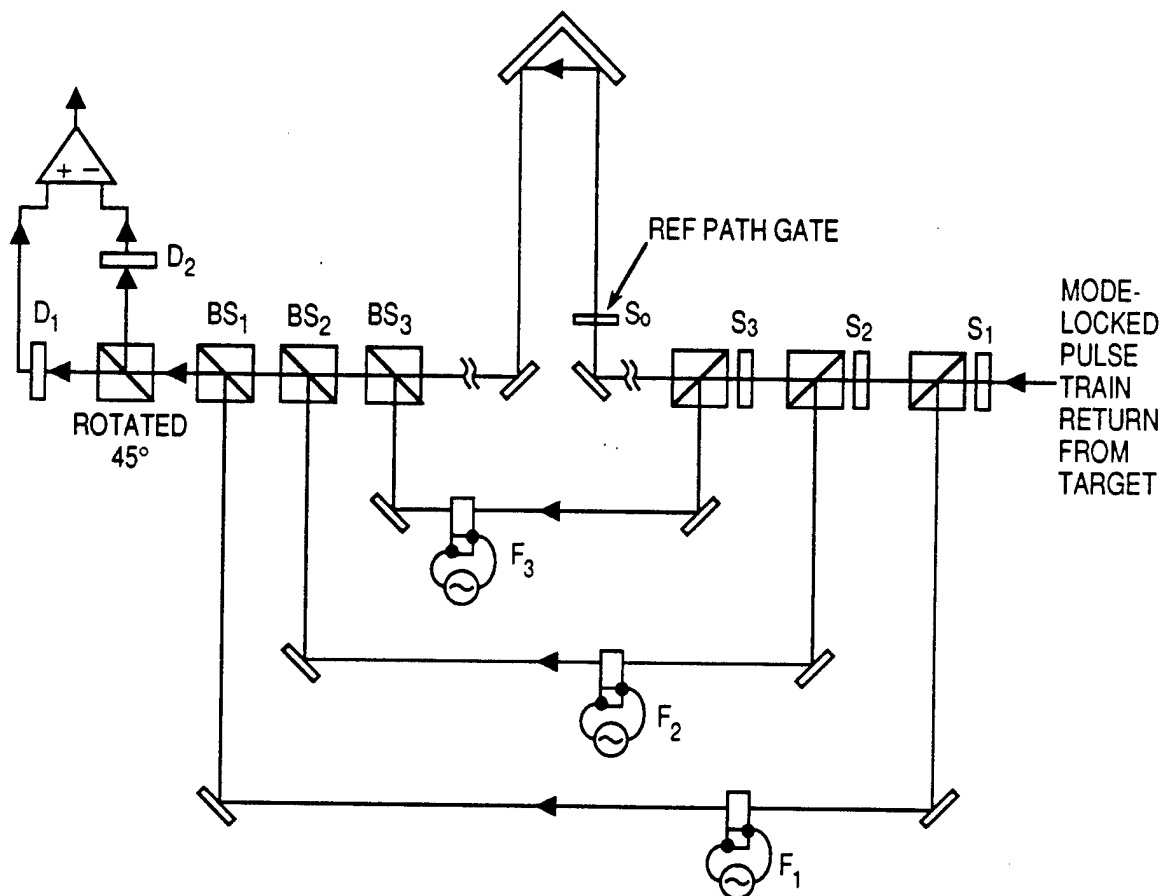
Figure 2-4.   A single (balanced) detection system with
frequency encoding of the range bins.

Another possible instrumentation is illustrated in Figure 2-5. A pair of Bragg cells services both the splitting and recombining (with the reference) of all image range cells. A series of acoustic pulses, whose frequency progressively changes in steps, is propagated down the cell. The timing is arranged such that each acoustic pulse arrives at the acousto-optic interaction volume in temporal coincidence with the optical image pulse return from a corresponding object range cell.

2.5 S/N ANALYSIS

We start by analyzing the basic multiple detector system of Figure 2-3. A single detector of this system is shown in Figure 2-6a while the more efficient balanced detector equivalent is shown in Figure 2-6b.

It is assumed that optical narrow band filters, together with range gating, will reduce the background photon count to a negligible level. It is further assumed that the reference signal is offset in frequency by 30 or 40 Mhz, as discussed in Section 2.1, such that the intermediate frequency amplifiers operate in a regime well above $1/f$ noise components. Thus, there is the potential for quantum limited performance if the reference is sufficiently bright. We also assume that the switching system of Figure 2-3 is essentially loss free. However, our equivalent local oscillator signal — the reference signal — must be split into Nr weaker components (with appropriate delays to service the Nr range cell returns. In our view, this is the fundamental S/N problem of this particular system. This limitation is analyzed in the paragraphs which follow.

If $(A_r)_{tot}$ is the total received field magnitude associated with a particular pulse return [of shape envelope $P(t)$] then the reference field available to any one range-bin detector is
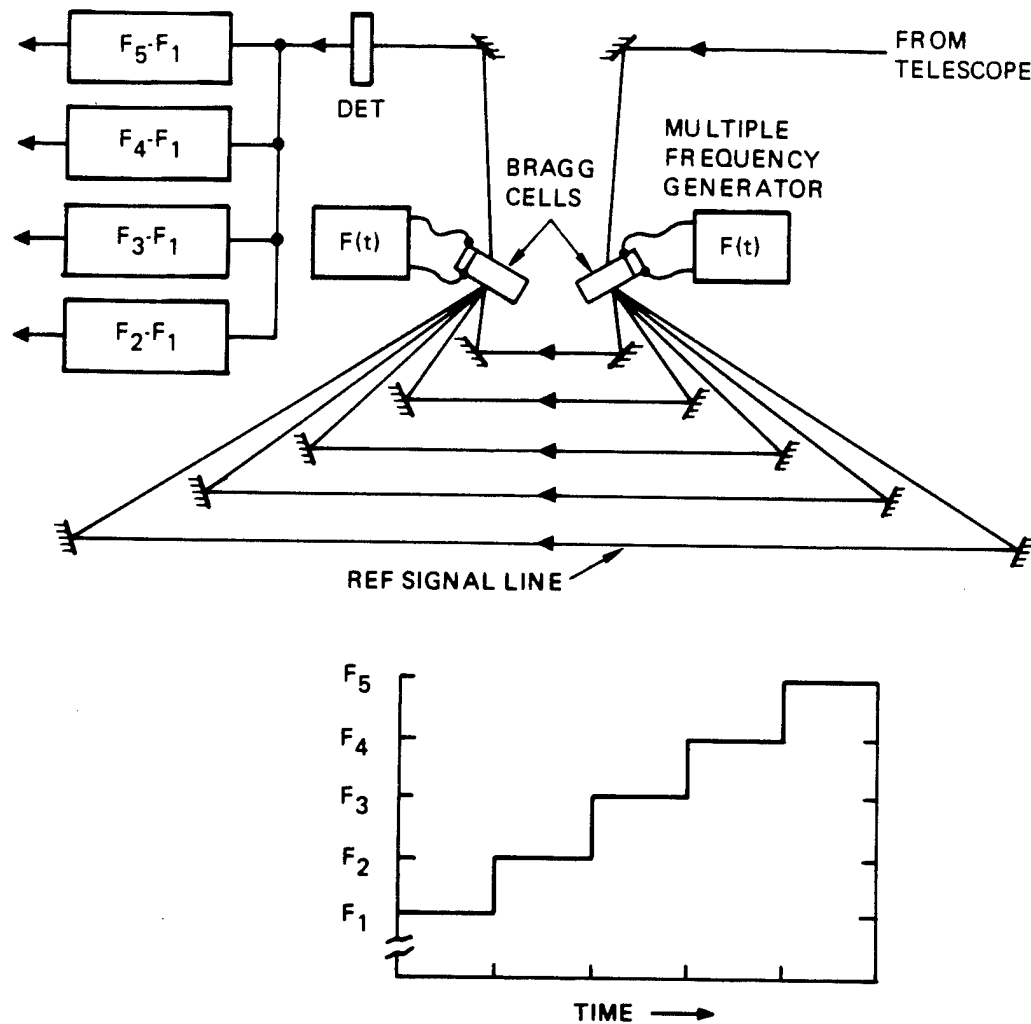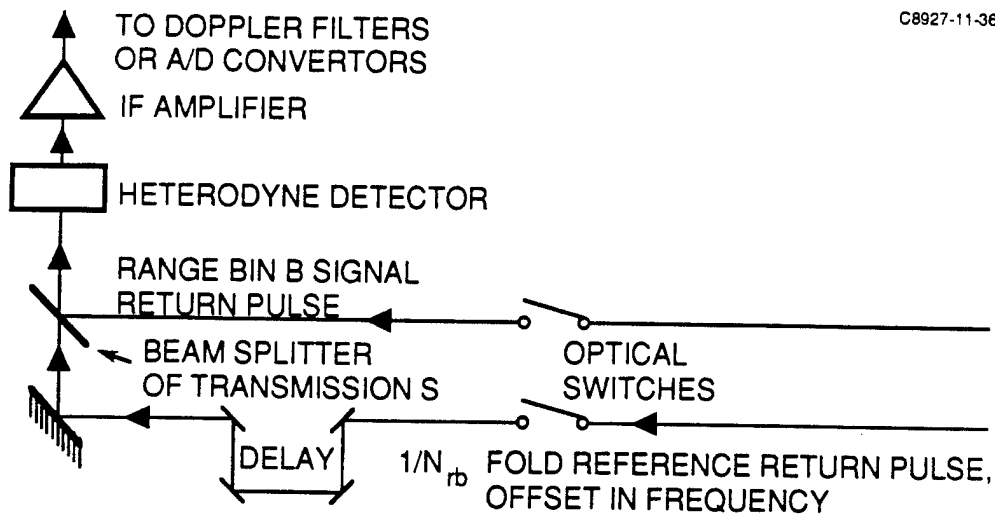
Figure 2-5.   High efficiency receiver with a single detector and frequency encoded range cells.

TO DOPPLER FILTERS
OR A/D CONVERTORS

IF AMPLIFIER

C8927-11-36

HETERODYNE DETECTOR

RANGE BIN B SIGNAL
RETURN PULSE

BEAM SPLITTER
OF TRANSMISSION S

OPTICAL
SWITCHES

DELAY

$1/N_{rb}$ FOLD REFERENCE RETURN PULSE,
OFFSET IN FREQUENCY

(a)

TO DOPPLER FILTERS
OR A/D CONVERTORS

+ −

b   a   IF AMPLIFIER

b   a   HETERODYNE DETECTORS

RANGE BIN B SIGNAL
RETURN PULSE

BEAM SPLITTER
OF TRANSMISSION S

OPTICAL
SWITCHES

DELAY

$1/N_{rb}$ FOLD REFERENCE RETURN PULSE,
OFFSET IN FREQUENCY

(b)

Figure 2-6.   Simplified detector systems employed for S/N
analysis.

20

$$U_r = \sqrt{S} A_{ref} e^{i\omega_r t} \tag{1a}$$

where S is the splitter (power) transmission ratio and

$$A_{ref} = \frac{(A_r)_{tot}}{\sqrt{N_{rb}}} \tag{1b}$$

where N_{rb} is the number of range bins (and detectors). The range gated signal return of any range bin as it reaches the detector is (omitting the differential phase shifts, which are not of concern here) given by

$$U_{SIG} = (\sqrt{1-S}) A_{SIG} e^{i\omega_{rb} t} \tag{2}$$

The signal detector current is given by

$$I_{det}(t) = P(t) \left[|U_{SIG}|^2 + |U_r|^2 + 2|U_r||U_{SIG}| \cos(\omega_r - \omega_{rb})t \right] \left(\frac{qe}{h\nu} \right) \tag{3}$$

where e is the electronic charge, q is the detector quantum efficiency, h is Plank's constant and ν is the frequency. This is of the same form as a conventional heterodyne detector where the reference field substitutes for the local oscillator field and we will borrow from the standard literature to define the S/N (power) ratio as the ratio of the average signal current squared divided by the expected noise current squared. The first two terms generate shot noise and the last term generates signal giving the conventional result

$$S/N = \left\{ \frac{|U_r|^2}{|U_r|^2 + |U_{sig}|^2} \right\} \left(\frac{q}{h\nu} \right) E_{det} \tag{4}$$

21

where E_{det} is the signal energy in the pulse $P(t)$, falling on the detector. In conventional heterodyne detection the splitter ratio S is chosen to be small and the local oscillator power is boosted to the point that it appreciably dominates the signal power, even allowing for the large splitter loss. This gives the quantum limited result

$$(S/N)_{QL} \overset{\circ}{=} \left(\frac{q}{h\nu}\right) E_{rec} \tag{5}$$

where E_{rec} is the <u>received</u> energy and virtually identical with E_{det}. The splitter ratio S, in conventional applications is small, and is not critical.

The result of Eq. (5) will be our standard of comparison for the RD-TRIMS system. For this system, upon substituting Eqs. (2) and (1a) into Eq. (4) and noting that $E_{det}=(1-S) E_{rec}$, the result is

$$S/N = \left[\frac{S \ R_{eff}(1-S)}{S \ R_{eff}+(1-S)}\right] \left(\frac{q}{h\nu}\right) E_{rec} \tag{6a}$$

where R_{eff} is a relative effective reference strength,

$$R_{eff} = \left(\frac{A_{ref}}{A_{sig}}\right)^2 = \frac{\left((Ar)_{tot}\right)^2}{N_{rb}\left(A_{sig}\right)^2} \tag{6b}$$

If the reference is a very bright glint, then quantum limited performance can be achieved. More realistically, the R_{eff} values which can be expected are of the order of unity. The splitter ratio for this system then becomes somewhat more critical. In all cases there is an optimum splitter ratio S which is

$$S_{opt} = \left[1 + \sqrt{R_{eff}} \right]^{-1} \qquad (7)$$

The associated (optimized) S/N ratio thus becomes

$$\left(S/N\right)_{opt} = \left[\frac{\sqrt{R_{eff}}}{1+\sqrt{R_{eff}}} \right]^{2} \left(S/N\right)_{QL} \qquad (8)$$

where $(S/N)_{QL}$ is the quantum limited S/N. The worst case which would be expected in practice is where the reference and image components are equally bright, that is

$$\left(R_{eff}\right)_{worst} = \left(N_{rb}\right)^{-1} \qquad (9)$$

giving, via Eq.(8) (for the best splitter ratio),

$$(S/N) = \left[\frac{1}{1+\left(N_{rb}\right)^{1/2}} \right]^{2} (S/N)_{QL} \qquad (10)$$

More realistically we expect to work with brighter references. As discussed in Section 2.3, the reference will often be chosen as a leading convex edge of some rounded surface or protrusion and with typical painted surfaces there will be an underlying weak specular component which will dominate the Lambertian components. Thus an order of magnitude enhancement in the reference ratio, $(A_{ref}/A_{SIG})^{2}$, is a reasonable expectation. This provides a signal to noise performance down by a factor of four (from quantum limited performance) as illustrated in Figure 2-7. Using a balanced detector system, as illustrated in Figure 2-6b, nearly restores the quantum limited performance. The single detector S/N performance assumes an optimum splitter ratio S while the balanced detector performance assumes a more
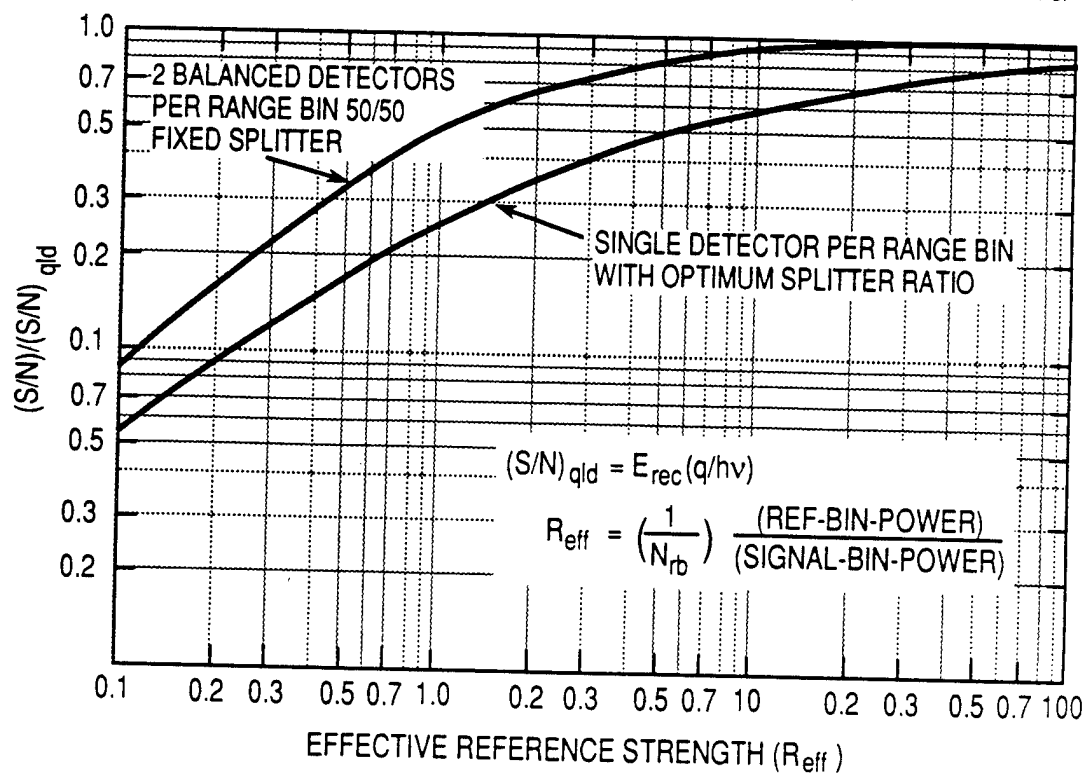
23

Figure 2-7. Normalized S/N performance of two types of RD-TRIMS detector configurations as a function of the effective reference strength.

practical, fixed (50/50) splitter (S=0.5). It is evident that for the important range of R_{eff} from 1 to 10 that the splitter ratio is not critical.

The results described up to this point are valid for a single pulse in the pulse train of the return fields. However, assuming that the differential Doppler shifts remain constant in time over the integration interval, these pulses may be coherently integrated, independently of drifts in the laser illuminator frequency. That is these pulses define a sinsoidal envelope whose frequency (and phase) is stationary over this interval. Thus (as in all coherent radars) it is the illuminator energy which is available over the measurement period that determines the S/N performance.

2.6 HIGH-SPEED ELECTRO-OPTIC SWITCHING

In the RD-TRIMS systems, the reference must be range-gate-selected from the ensemble of the image object reflectivity cell returns via a high-speed, high-PRF switch with good switching efficiency. Similarly, other switches of the same general type are required to perform the range-gate selection of the image cell signals in order to sequence them through the proper optical-path delay lines. For this purpose, we have elected to employ an optical switch as our main line approach, for the following reasons:

(1) Such a switch is required if Doppler-tracking local oscillators are to be avoided.

(2) Low bandwidth detectors may be employed. Therefore the detectors need not sacrifice sensitivity for response speed.

(3) As discussed above, the optical gating can protect the detector from excess shot noise generated by clouds or other background sources.

These optical switches must be capable of repetitive operation at a rate that matches the highest PRF of the laser illuminator. This presents a challenging technology issue, and solutions to the design problems of such a switch are briefly considered in this section. The switches shown in Figure 2-3 were bulk-wave electro-optic (EO) switches. These switches easily achieve the desired subnanosecond response speeds, if they can be driven with the appropriate short-pulse, high-PRF, high-voltage waveforms. The driver presents a nontrivial problem and we propose a novel solution which, to our knowledge, has never been tried. Our solution, as illustrated in Figure 2-8, is to embed the electro-optic crystal in a TEM transmission line that is resonant at all the harmonics of the periodic waveform required to activate the polarization rotation of the EO crystal. The advantage of this approach is power conservation. That is, the reactive energy required to charge the EO electrode capacitance is substantially recovered by the resonant nature of the system. The electrical drive may consist of either discrete sinusoids, representing the discrete Fourier components of the waveform (as illustrated in Figure 2-8), or of the desired time domain waveform itself.

This approach appears to be practical only for high PRF modes (PRFs exceeding 40 MHz) because of transmission line lengths and because of the large number of modes required at low PRFs.

Yet another approach to high-speed switching employs integrated-optic waveguide-coupling switches, as illustrated in Figure 2-9. This particular implementation is a multiple detector system which is very similar to the system of Figure 2-3. Since the required switching voltages are quite low with guided-wave devices (a few volts), driver power and dissipation are not major issues, and a wide variety of PRF waveforms are readily accommodated. With this approach, fiber-optic delay lines provide the most practical and compact

OPTICAL BEAM

STRIP
LINE
RESONATOR

DIELECTRIC LOADING

f_1 $3f_1$ $5f_1$ $7f_1$

POCKEL
CELL

SUMMATION OF
FIRST AND
THIRD HARMONICS
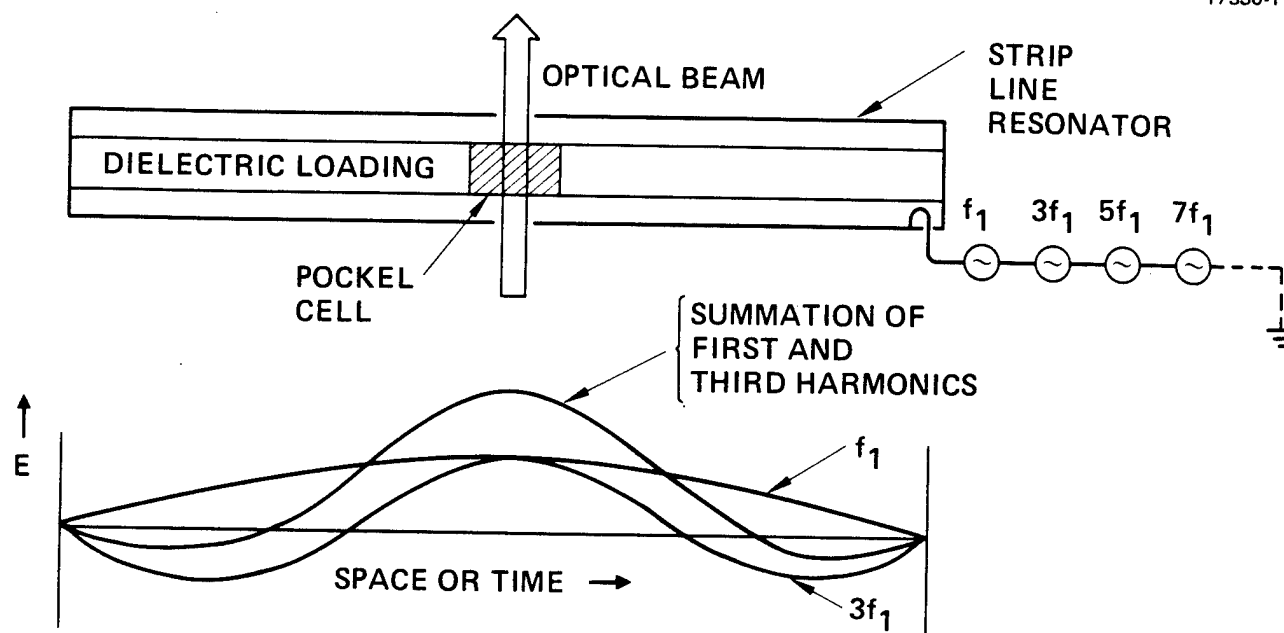
f_1

E

SPACE OR TIME →
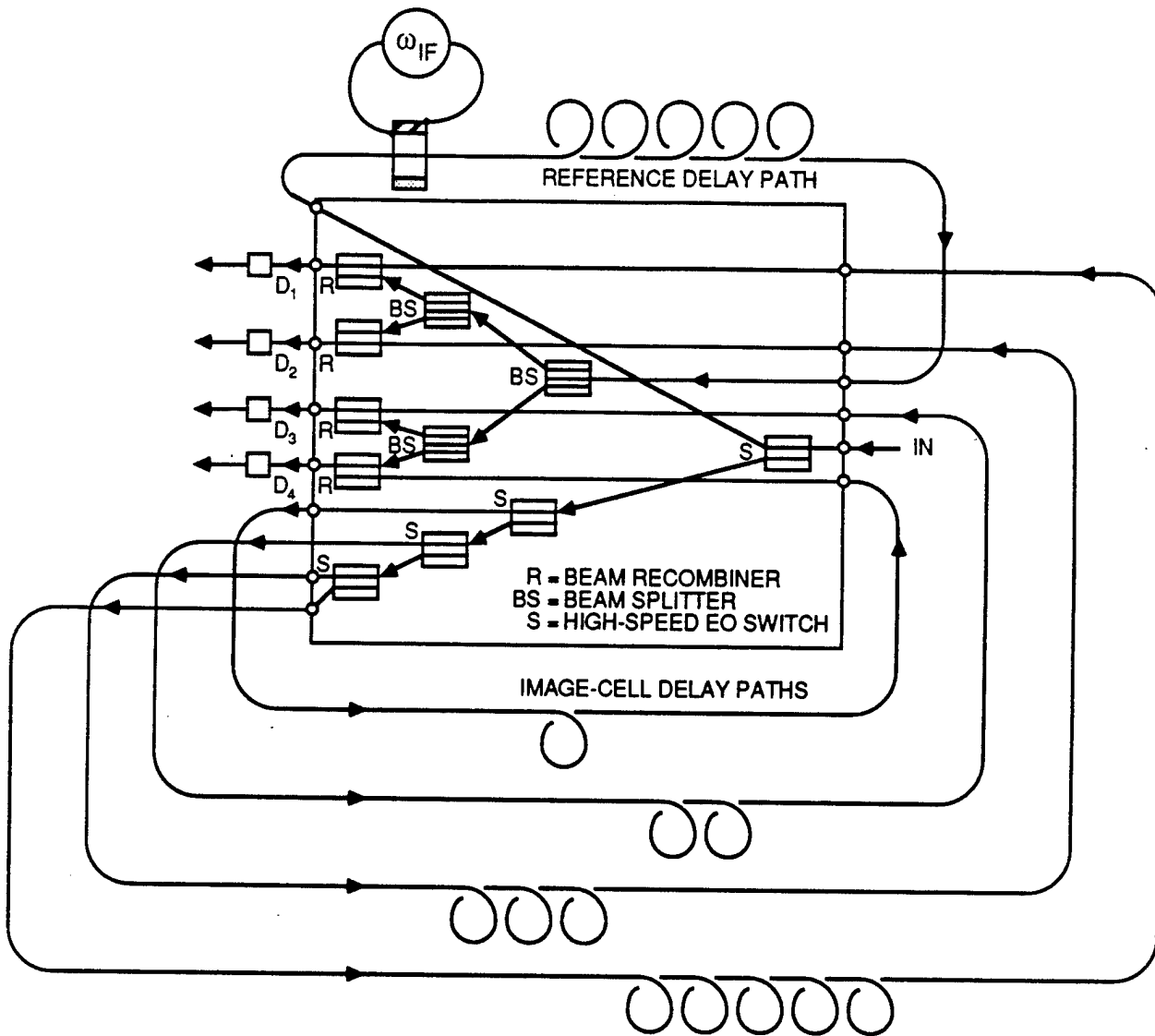
$3f_1$

Figure 2-8.   "Mode-locked" E.O. switch

Figure 2-9. An integrated optics RD-TRIMS receiver of the space-domain range-gating class.

approach to equalizing the reference and image cell path delays. It is an open question as to whether these guided-wave devices can achieve comparible thruput optical efficiency to the free space switches.

SECTION 3

A BRIEF COMPARISON OF NATURE OF CONVENTIONAL AND RD IMAGES

Figure 3-1a shows the cross-section of a flat, plate-like object with a raised stripe (boss) and its conventional (angle-angle) image. If the object is slowly rotating or translating, then there is a spread in Doppler shifts in the returns from across the object that permit one to form a range Doppler "image" as well. This image is illustrated in 3-1b, for the case with translation of the object perpendicular to the illumination and parallel to the plate. A prime function of an RD system is to form such an image; ideally a plot of object reflectivity versus Doppler frequency shift (or Doppler bin number) and range (or range bin number). A secondary function is described below. This RD imagery function is analogous to that of conventional angle-angle imaging systems, and the RD image may have a strong resemblance to the corresponding angle-angle image, as in the illustrated case. Alternatively, with other objects and motions the character of the RD image may be quite different from that of the corresponding angle-angle image, as we will see in Section 4.3. Further, the RD image may sometimes exhibit ambiguities which would be absent in the conventional image.

However, if we extend the concept of imaging to encompass three-dimensional object characterization, then the RD image may present fewer ambiguities than the conventional image, since the conventional angle-angle image (with monostatic long-pulse illumination) contains no depth information. In the above example, a conceptual, ideal image, free of speckle and noise, was generated from an object where the plate and its boss had the same reflectivity — perhaps painted with "flat" paint. How can the information in our images clue us to the presence of the raised, uniform reflectivity boss, rather than a dark stripe on the object? Since one face of the boss is normal to the line

C8927-11-40

CONVENTIONAL IMAGE

a

C8927-11-33
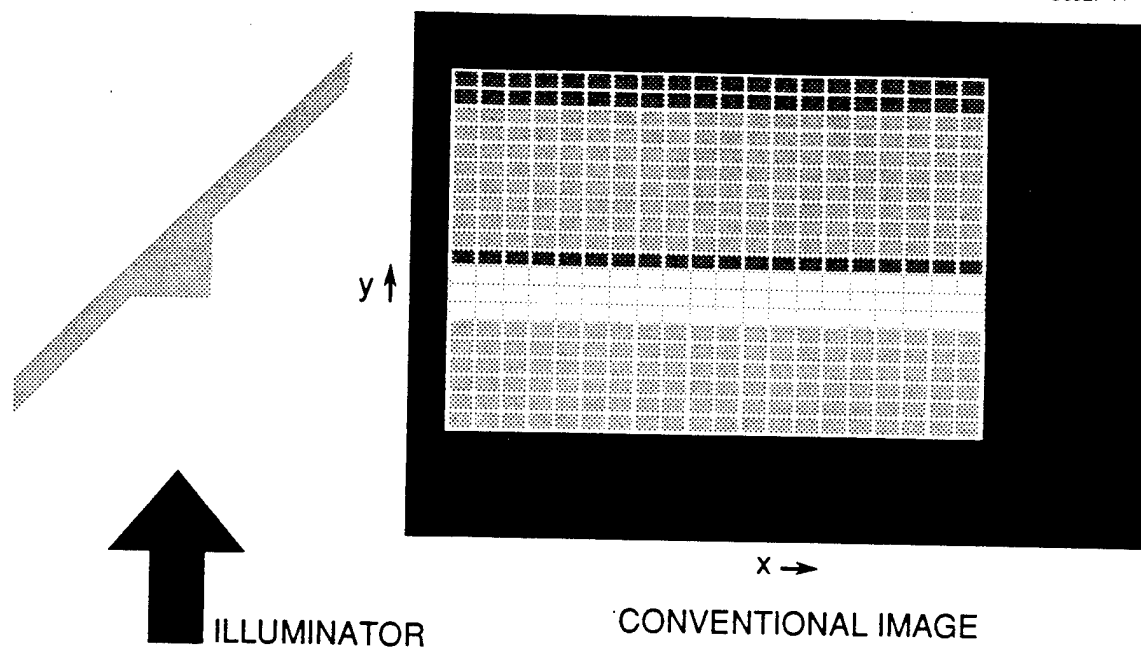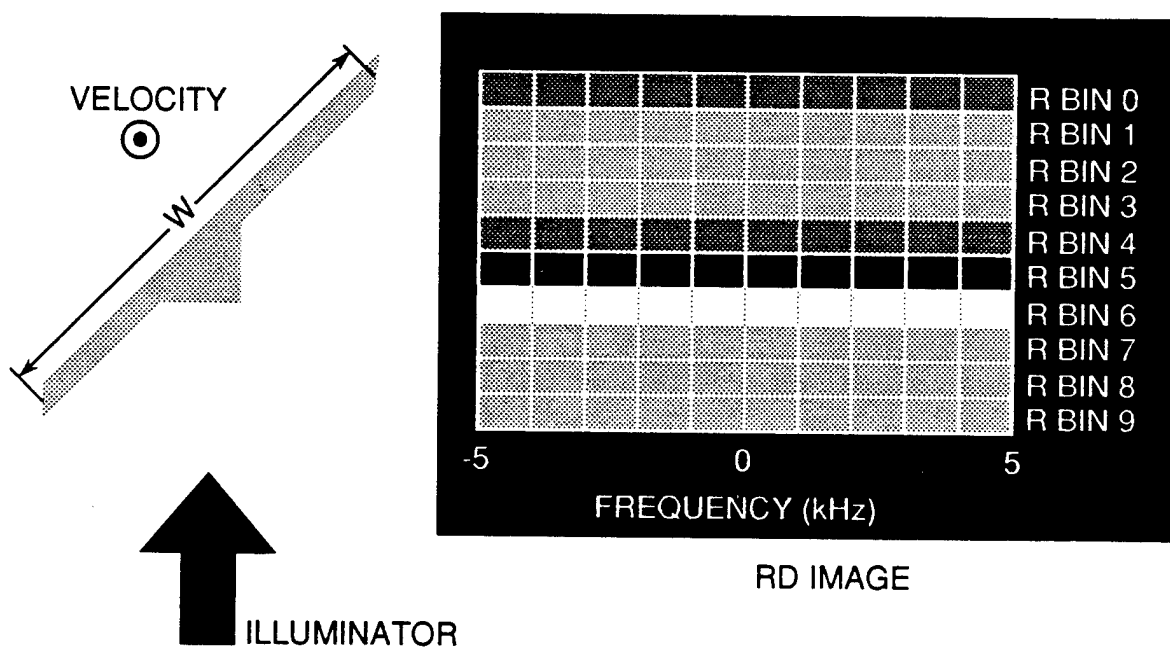
RD IMAGE

b

Figure 3-1. A comparison of conventional and RD imaging
systems.

31

of sight and Lambertian scattering is assumed, a brighter band
appears at this location in the RD image, as occurs as well with
the corresponding angle-angle image. There is one obvious
difference between the images of Figures 3-1a and 3-1b. The
black band which falls just above the white-band, boss-face RD
"image" (only) is a result of missing reflections from that
range cell which matches the other (non-reflecting) face of the
boss. This black band offers a strong clue that a boss may have
been present (the white band alone could have more simply
resulted from a whiter stripe at the boss location). There is
no comparably strong clue in the corresponding angle-angle
image. Further, the ordering of the light and dark bands
suggest a raised object (a boss) rather than a depression.

Other 3-D object information is readily available from the
RD image. The average plate angle of inclination information
(45°) is available from the RD image data (assuming that the
plate velocity or rotation rate is known) while it is lacking in
the angle-angle image information. Still further, the true
object width, w, is available from the RD image, whereas only
the projected width is available from the angle-angle image.
Thus, we have provided a simple example where the RD image is
less ambiguous than the angle-angle image, with respect to a
number of important object features.

Additionally, the RD image may contain important time-
varying signature information which has no counterpart in angle-
angle imaging. If we consider the same object as in Figure 3-1
and expand the Doppler frequency scale (which requires
additional Doppler filters or computer processing), say from ±5
to ±25 kHz, then the new RD image may appear to exhibit new
features as illustrated on the right side of Figure 3-2.
Specifically, one observes additional extended spectral returns
which appear to be harmonically related, and these occur in one
range bin only. Further, these broad-band (harmonic) returns
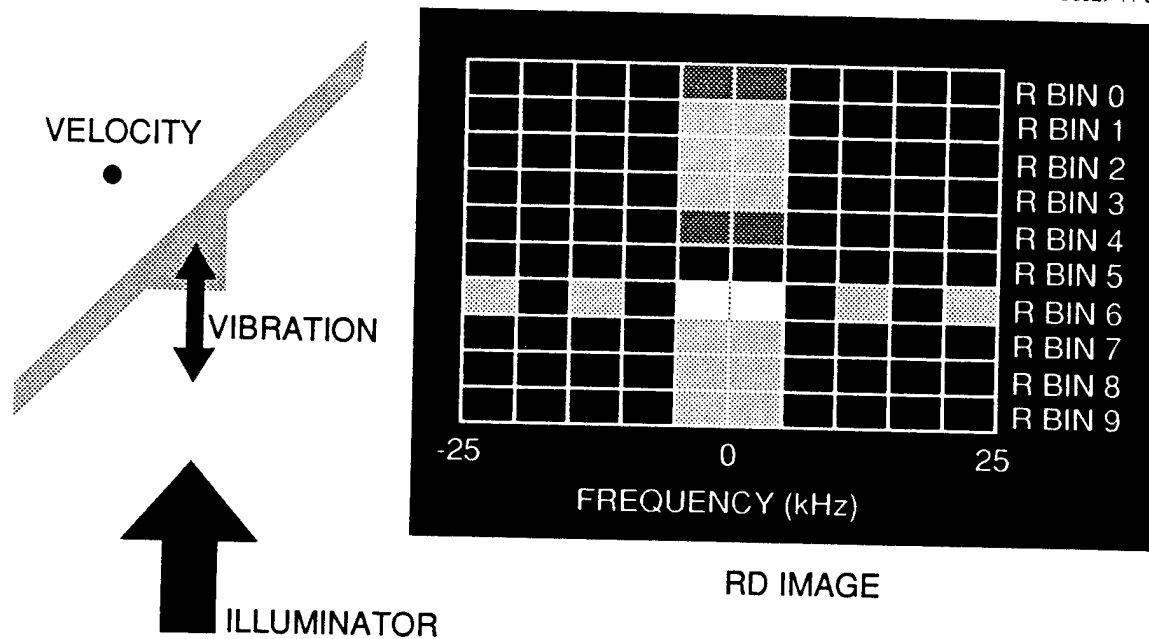are occurring at that range which we just associated with a

Figure 3-2.   Vibration signature information available in a RD image.

possible boss. Thus we expect that the boss (or some portion of it) is probably vibrating at a frequency of around 5 kHz, with relatively low amplitude (if the Doppler spectrum is not rich in harmonics, as illustrated).

Computer simulations indicating the signature information which is available from a vibrating ball are presented in Section 4.3.

SECTION 4

SYSTEM MODELING

4.1 OVERVIEW OF MODELING APPROACHES

We have developed computer models for two example objects. Initial calculations modeled a slowly rotating or translating, plate-like object of variable reflectivity. Note that there is an apparent rotation about the line-of-sight associated even for a purely translating flat plate. A subsequent code was developed to model a translating, vibrating or rotating sphere.

Both models represented the target as a series of discrete wide-angle scattering sites, with each site having small (a few λ to 0.1 mm) random height perturbations above the plate or spherical surface. The return wave was assumed to be spatially uniform across the receiver aperture. That is, the receiver aperture does not resolve the objects. Phasing variation errors which might be introduced by the atmosphere, for example, are assumed to match for the reference and image fields and are not explicitly modeled.

For each selected range bin and pulse- or time-step, the received complex field is mixed with (or beat against) a similar reference return, with the process being repeated over a series of appropriate, equally spaced time-steps. Each time-step in the sequential codes represents one temporal sample of the intermediate frequency. The signal from this sequence of time steps was transformed, via a Discrete Fourier Transform (DFT) or a Fast Fourier Transform (FFT), into a characteristic Doppler signature for that range.

The number of scattering sites range from less than 80 for the flat-plate model to several hundred for the spherical model. From 63 to 256 temporal samples were employed in both cases and the temporal samples were apodized in both cases, but with different weighting functions.
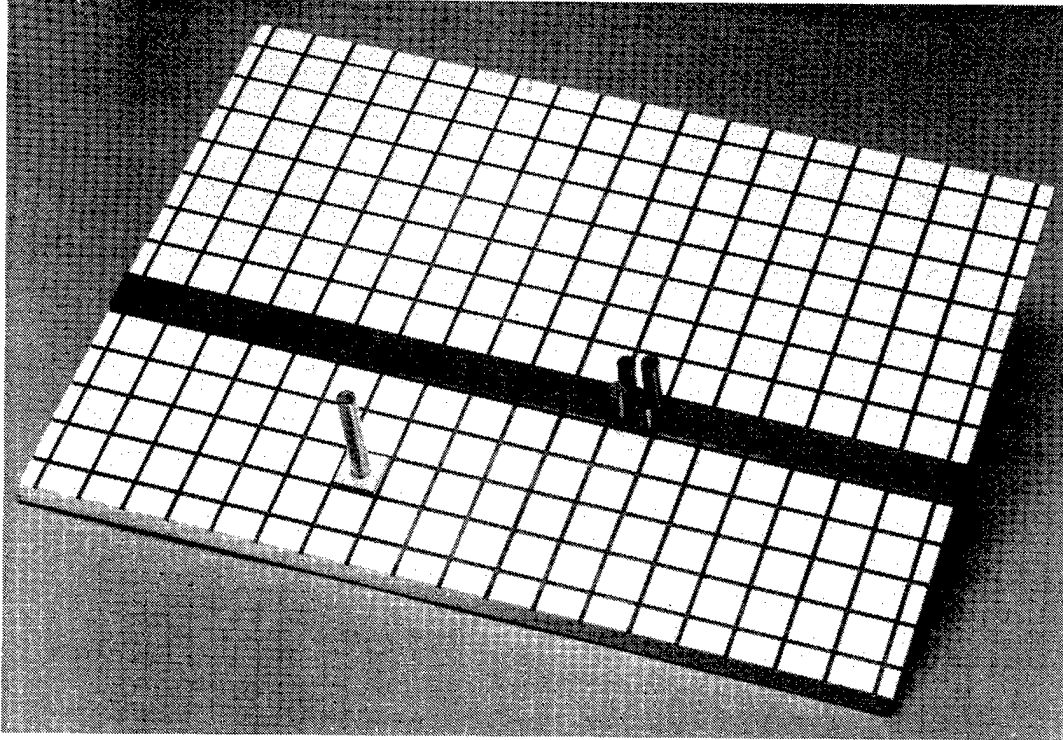
4.1.1 Flat Plate Model

Figure 4-1a is a picture of a flat-plate model which is conceptually divided into image pixels which are of one range-bin resolution in depth and one Doppler bin resolution in width. The dark band illustrates a single range bin. Each resolution bin in this model consisted of five to ten equal-reflectivity, equally-spaced scattering sites of random height above the flat reference plane. This is illustrated for one resolution cell by the five posts in Figure 4-1a. A single high post represents a typical "ideal" reference. A wide range of reflectivities were employed from resolution cell to resolution cell. An edge view of this model is illustrated in Figure 4-1b.
The flat-plate computer model was used to investigate the effects of speckle and of an extended reference reflector. Since, as discussed in Section 3, the translating flat plate, when inclined for oblique incidence of the illuminator beam, produces essentially the same type of image as angle-angle imaging, it was possible to directly compare these images for speckle effects. These simulations were run on a desk top computer in BASIC.

4.1.2 Sphere Model

Although numerical issues such as signal-to-noise, speckle, and pattern fidelity can be addressed simply with the canted, translating, 1-d flat plate model described above, human interpretability of the images from more realistic complex objects is best addressed by simulation of 3 dimensional objects undergoing various combinations of translation and rotation and vibration. We used the simplest 3-d base surface geometry - a sphere - and computed the images formed by simply-shaped

a. Slant View of Model

SIGNAL PULSE

SCATTERED CENTERS AT RANDOM HEIGHTS

REF PULSE
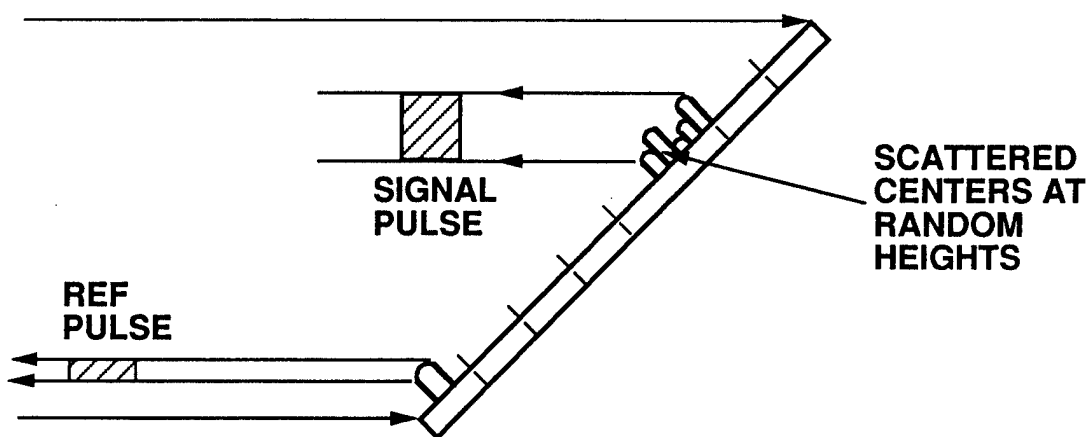
b. Edge View of Model

Figure 4-1. Flat-plate target modeling geometry.

reflectors reflecting elements or scatter sites of uniform reflectivity distributed in various simple patterns on the sphere.

The impact of extended reference reflectors and noise on these images was also investigated. Sources of noise included random background scatterers, detector dark current, overall low light levels, and distribution of low light levels between the reference and range reflections.

The simulation code is written in FORTRAN and is broken into subroutine sections so that modifications to handle other objects and other reflection patterns do not entail major rewriting. Each reflection point on the surface is assigned an initial set of coordinates, an initial range bin, and an initial optical path distance (OPD) to a chosen reference point. Time steps between illuminating laser pulses are then determined by the sampling rate requirements of the largest anticipated doppler shift. The code keeps track of the changing coordinates, range bin, and OPD of each reflector. The reflected wave from the reference range (generally the near edge of the sphere) and from up to 20 other ranges is calculated and saved for later processing. Processing includes modulation and splitting of the reference wave, calculation of the interference intensity on each of the range bin detectors, filtering, addition of noise, and frequency analysis of each pulse train. Finally, a two dimensional image is formed by the display of range bin versus frequency.

The first part of our study was aimed at demonstrating the type of patterns obtained in imaging scatter distributions falling on lines or bands of reflectors on a rotating, translating, or vibrating sphere. Subsequently, we looked at sources of image degradation, such as extended reference reflectors and noise at low light levels.

38

4.2 Flat Plate Modeling Results

The translating or rotating inclined plate model was selected for our initial simulations both because it is relatively easy to model and it permits ready comparison to angle-angle imaging.

Since each range cell of the inclined plate model gives essentially the same type of image performance as every other range cell, it was not required to incorporate range gating into this model.

Each nominal RD resolution cell was chosen to have 5-10 uniformly spaced scattering centers of equal reflectivity, randomly distributed in height (with uniform probability distribution) between 0 and H_{max} above the top plane of the plate. The reflectivity of each RD cell is generally variable from cell-to-cell and this variability contains the image information (as in conventional) angle-angle imaging. Typically nine Doppler resolutions cells were employed in a single range bin.

The optical path differences experienced by a reflected plane wave, scattered from each of N scattering "image" sites, back to a point receiver, are computed and these are used to compute the phases of the N complex received fields associated with each scatterer. The N fields are then summed to produce the composite received "image" field. This is repeated for each new object position, produced by a discrete object motion, during each equally spaced time-step. This process is then repeated for the reference (which incompases 1 to 10 scattering sites), the two complex fields are multiplied at every sample time and the real part is used to represent a sample of the intermediate frequency output.

The "intermediate frequency" employed in these simulations is simply the natural Doppler offset provided by the displacement between the reference element(s) and the image elements.

Figure 4-2a illustrates the geometry which was employed to compute the optical path differences and hence the differential phase shifts for each scattering site. If we reference to the left edge (scattering site "0"), the optical path difference OPD(s) to the sth scattering sites is given by

$$\overline{OPD}(s) = sD \sin (\theta_i) + H(s) \cos (\theta_i) \qquad (4-1)$$

where D is the separation between scatter sites, H(s) is the height of the sth scatter site above the plane, and θ_i is the incidence angle. The associated optical phase shift difference is

$$\Delta\phi(s) = 2k \ \overline{OPD}(s) \qquad (4-2)$$

where

$$k = 2\pi/\lambda$$

Since we assume the object to be translating above the ground with uniform velocity v, the incidence angle θ_i has a temporal dependence which, as illustrated in Figure 4-2b, is given by

$$\theta_i(t) = \tan^{-1} \left[\frac{v \ t}{0}\right] \qquad (4-3)$$

where the temporal origin is taken at the overhead (or closest pass) position and 0 is the distance to the object at that time. For visible RD systems the images can be generated in a time period which is sufficiently short that $\theta_i(t)$ is substantially linear in t over the signal integration time. An excellent approximation to Eq. (4-3) is then

SCATTERED SITE "O"

D_{obj}

B

D   D   D

H(1)   H(2)   H(s)

θ_i

$\overline{OPD}(s)$

$\overline{\Delta OPD}(s) = B \sin(\theta_i)$

$B = sD + H(s)/Tan(\theta_i)$

θ_i

(a)

v

x = vt   t = O

D_{obj}

θ_i RECEIVER SITE
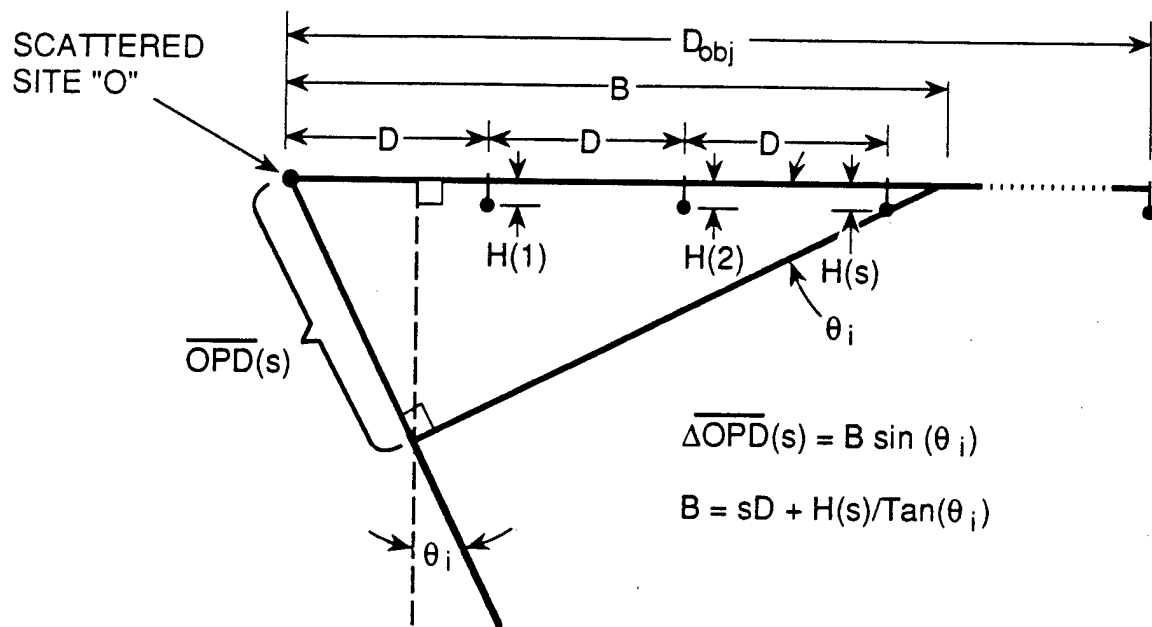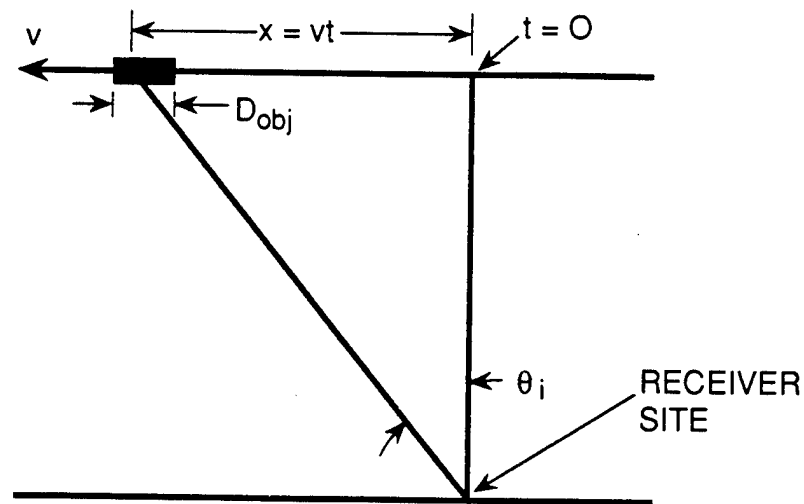
(b)

Figure 4-2.   Geometry for the calculation of the differential phase shifts generated by each scattering site.

41

$$\theta_i(T_o + \Delta t) \overset{\bullet}{=} \theta_i(T_o) + \left[\frac{\partial \theta_i(t)}{\partial t}\right] \Delta t \qquad (4\text{-}4a)$$

where T_o is the time where the imaging pulses start to be accumulated and Δt is the time interval of an arbitrary pulse in the imaging sequence pulse train. Eq. (4-4a) becomes, upon substitution from Eq. (4-3).

$$\Phi_i(T_o + \Delta t) \overset{\bullet}{=} \Phi_i(T_o) + \left[\frac{v\Delta t}{0}\right] \cos^2 \theta_i \qquad (4\text{-}4b)$$

Thus, for the small Δt of interest here

$$\sin \Phi_i \overset{\bullet}{=} \left[\frac{v_{eff} \Delta T}{0}\right] \cos(\Phi_i(T_o)) + \sin(\Phi_i(T_o)) \qquad (4\text{-}5a)$$

$$\cos \Phi_i \overset{\bullet}{=} \cos(\Phi_i(T_o)) - \left[\frac{v_{eff} \Delta T}{0}\right] \sin(\Phi_i(T_o)) \qquad (4\text{-}5b)$$

The temporally varying parts of $\Delta\Phi(s)$ are thus

$$\Delta\Phi(s,t) = 2k\left\{ s D\left[-\frac{v_{eff} \Delta T}{0}\right]\cos \Phi_i(T_o) + H(s)\left[\frac{v_{eff} \Delta T}{0}\right]\sin \phi_i(T_o)\right\} \qquad (4\text{-}6)$$

For the cases we will consider, $s D \gg H(s)$ and $\cos \theta_i \geq \sin \theta_i$ so that the first term dominates and thus the $H(s)$ variation substantially contribute only to speckle and not to the Doppler signature. Thus, rather than computing the sines and cosines of (4-1) at every step, we use the much faster approximation

$$\Delta\Phi(s,t) = 2k\left\{ sD\left[\frac{v\Delta T}{0}\right]\cos^3[\theta_i(T_o)] + H(s)\cos[\theta_i(T_o)]\right\} \quad (4\text{-}7)$$

This equation also permits one to estimate the total differential Doppler spread which determines the minimum required sampling rate. Specifically this Doppler spread is

$$\Delta\nu_{dopp} = \frac{1}{2\pi}\left(\frac{d\Phi}{dt}\right)^{\bullet} \doteq \left(\frac{1}{2\pi}\right)\left(\frac{\Delta\Phi(s_{max},t')}{\Delta T}\right)$$

$$= \frac{2v}{\lambda}\left[\frac{D_{obj}}{0}\right]\cos^3\Phi_i(T_o) \quad (4\text{-}8)$$

where

$$D_{obj} = s_{max}\,D$$

4.2.1 RD Imaging Examples

Our canonic imaging example employs a 25 cm plate like object (after Figure 4-1) in a 300 km orbit, with a velocity of 7 km/sec. A single range slice, this object is modeled with five scattering sites per resolution cell and 8 to 10 resolution cells (per range bin), as illustrated on the RHS of Figure 4-3(a). The color or shading of the scattering sites depicts reflectivity, according to the scale on the left-hand-side, while the height distribution (normalized to H_{max}) illustrates the surface roughness. The reference is at the extreme left of the RHS half of the box and in this particular case consists of a single scattering site, illustrated by a single bar. One of the image cells (at the extreme right) has also been formed with a single scattering site in order to directly exhibit the point spread function of the imaging system. The middle box (b) of Figure 4-3 shows the discrete temporal samples of the beat (between the reference and image cell returns) as black lines. The bottom box (c) is a montage of several types of related spectral and image information, laid out to facilitate several
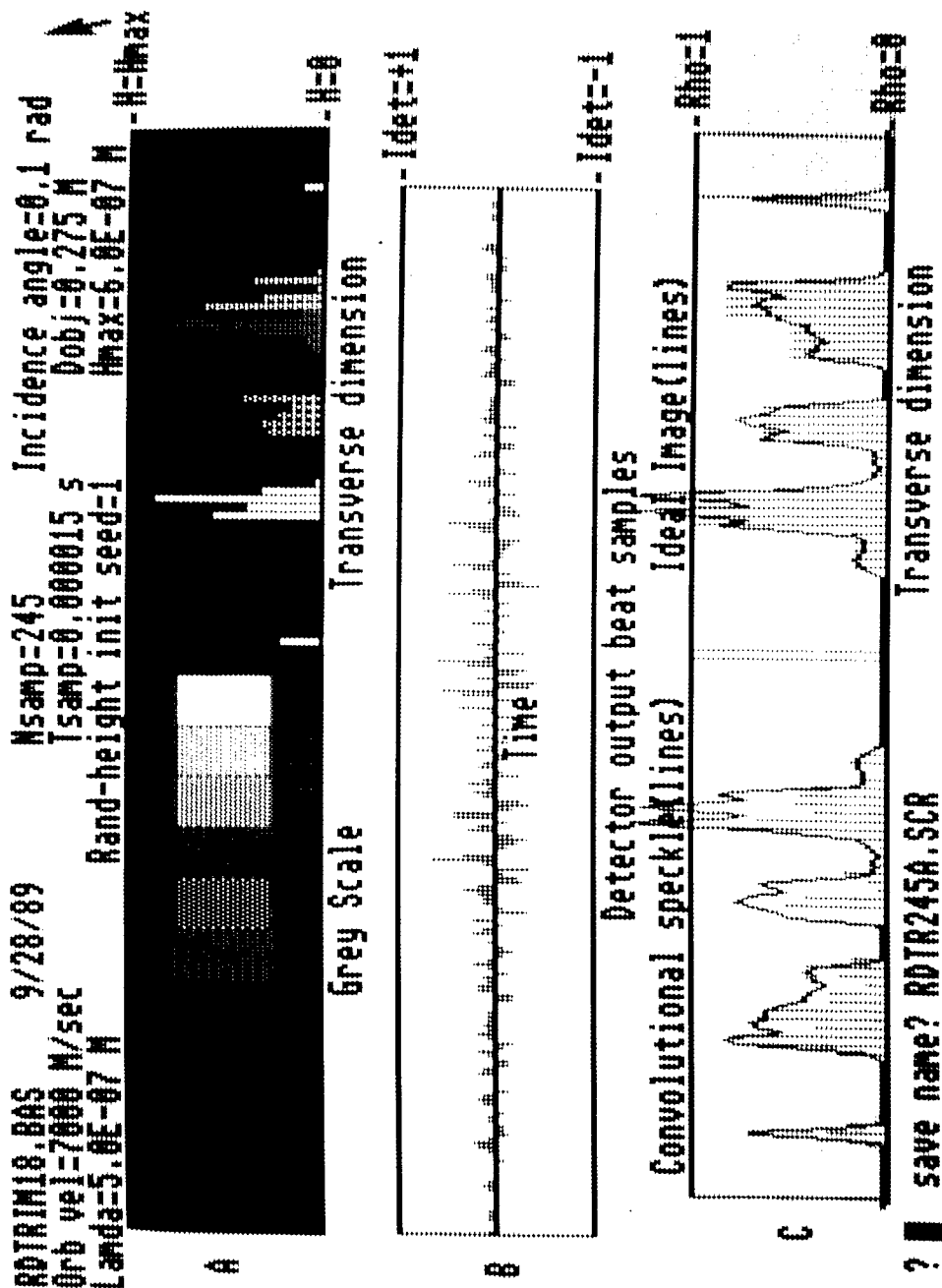
RDTRIM10.BAS   9/28/89   Nsamp=245   Incidence angle=0.1 rad
Orb vel=7000 M/sec   Tsamp=0.000015 S   Dobj=0.275 M
Lamda=5.0E-07 M   Rand-height init seed=1   Max=6.0E-07 M   H=Hmax   H=0

Grey Scale   Transverse dimension

Time   Idet=+1   Idet=-1

Detector output beat samples

Convolutional speckle(Klines)   Ideal Image(lines)   Transverse dimension   Rho=1   Rho=0

? save name? RDTR245A.SCR

A
B
C
?

Figure 4-3.   Flat-plate RD single-range cell image, wherein a relatively small number of discrete sites of varying intensity are encompassed by a single Doppler bin. Minimal speckling occurs and image fidelity is excellent.

types of imaging comparisons. The black lines on the right side represent the discrete scattering sites in alignment with (a). However, in box (c) the height of the lines represents the reflectivity of the sites. These lines thus depict the "ideal" image reflectivity as a function of transverse dimension or Doppler Shift of a RD imaging system with adequate frequency resolution to nearly resolve the individual scattering sites. This would also be the image obtainable with an ideal angle-angle imaging system with adequate resolution. In both cases no speckle effects would exist. In either case if the imaging system were of lower resolution such that the point spread function encompassed several point scatterers (of varying height), each image cell would experience interference between the returns from neighboring scattering sites, thereby generating a speckled image. In Figure 4-3c, the RD point spread function is just wide enough to generate a minimal interference and a weakly speckled image, as shown by the continuous black curve (the true spectrum generated via the samples of 4-3b). The red bars on the LHS of (c) depicts the image which would be produced by an angle-angle imaging system operating on this same object, but without motion. Each line can be conceived as representing the output of a particular detector in an imaging array. A sinc-like, angle-angle, point spread function is assumed and only a cross section of the image plane is illustrated, that cross section which corresponds to the same scattering sites selected by the range bin of the RD system. The speckled character of the image is again evident. The black curve of the LHS is a mirror image of the RD image spectrum for comparison purposes. Additional height distributions produced similar low-speckle images.

In Figure 4-4 we have illustrated a system with about 1/4 the integration time compared to that in Figure 4-3. Accordingly, the Doppler resolution is correspondingly reduced and the speckle variations are enhanced as a consequence of the extended interference effects.
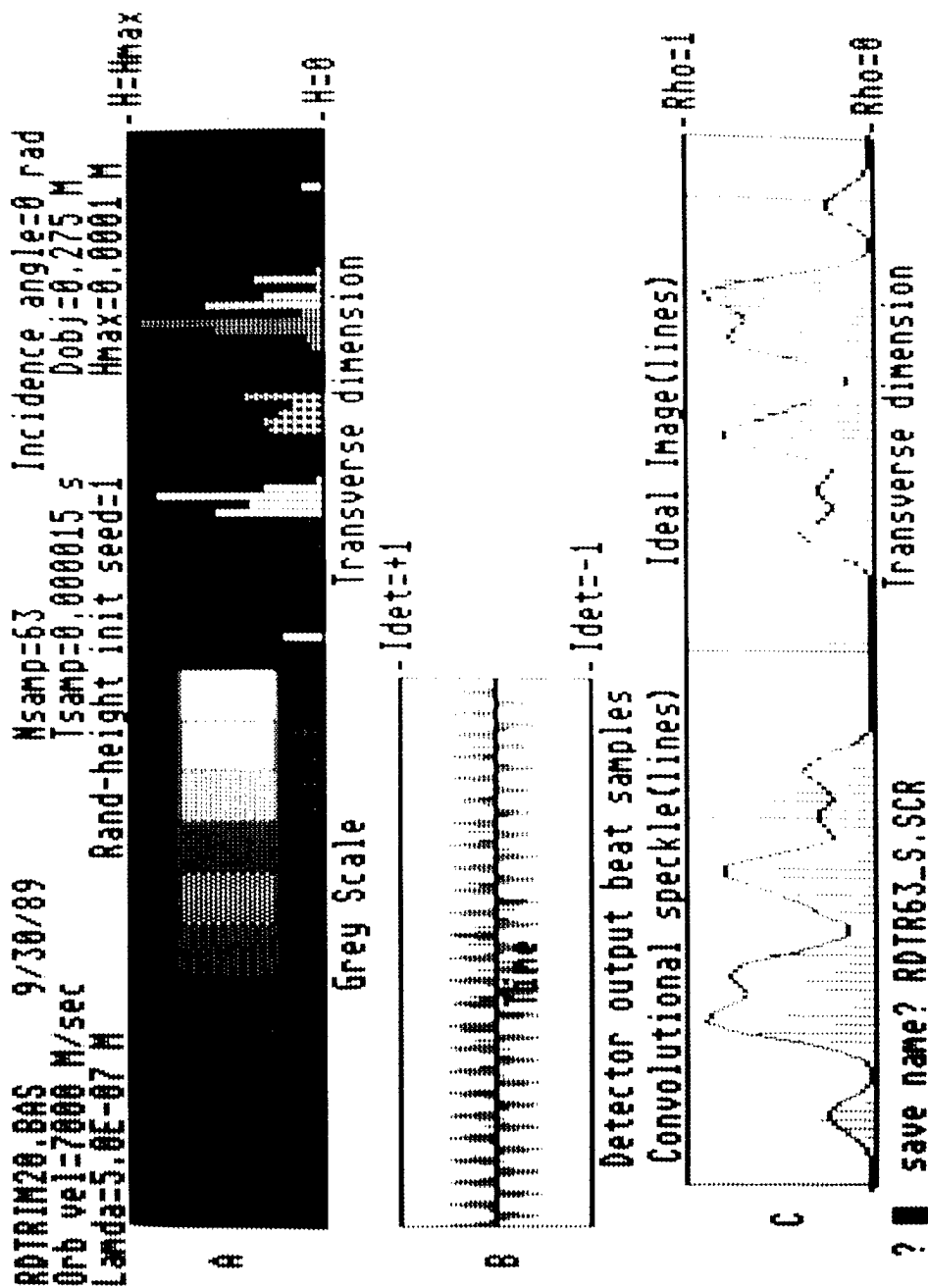
Figure 4-4. Flat-plate RD image, wherein the point-spread Doppler resolution is reduced as a consequence of the reduced integration time (e.g. reduced number of temporal samples). Speckle effects are enhanced since more scatter sites contribute to the scattering captured within the Doppler bin.

The impact of extended references was next explored. It was expected that this would result in a convolutional smearing of the RD images, and this was observed. What was not anticipated was the introduction of a new form of speckle as illustrated in Figures 4-5 (with a three scattering site reference) and Figures 4-6 (with a five scattering site reference). We believe the cause to be in the nature of a coherent convolution, wherein the various components which sum to form the convolution add with random phasing. We will call this effect "convolution speckle".

4.3 SPHERE MODELING RESULTS

In this section we describe the code used to simulate the RD-TRIMS images of scattering sites clustered in simple lines or bands and circles, together with randomly scattered points on a a rotating, translating, or vibrating sphere. A general discussion of the code is given below. This is followed by a summary of the results in Section 5.

4.3.1 Modeling Details

4.3.1.1 Reflector pattern setup. The patterns to be imaged were composed of a collection of point reflectors on the hemisphere facing the laser illuminator. A modifiable subroutine defines the position, height, and reflectivity of each point. The usual choices were uniform reflectivity and random height above the sphere in the range of 0 to 0.1 mm. Scatter site coordinates were chosen randomly (not equally spaced) over either the visible area of the sphere or along specified lines and circles on the sphere's surface. The reference reflector scatter sites were placed at random positions within the reference range.

47
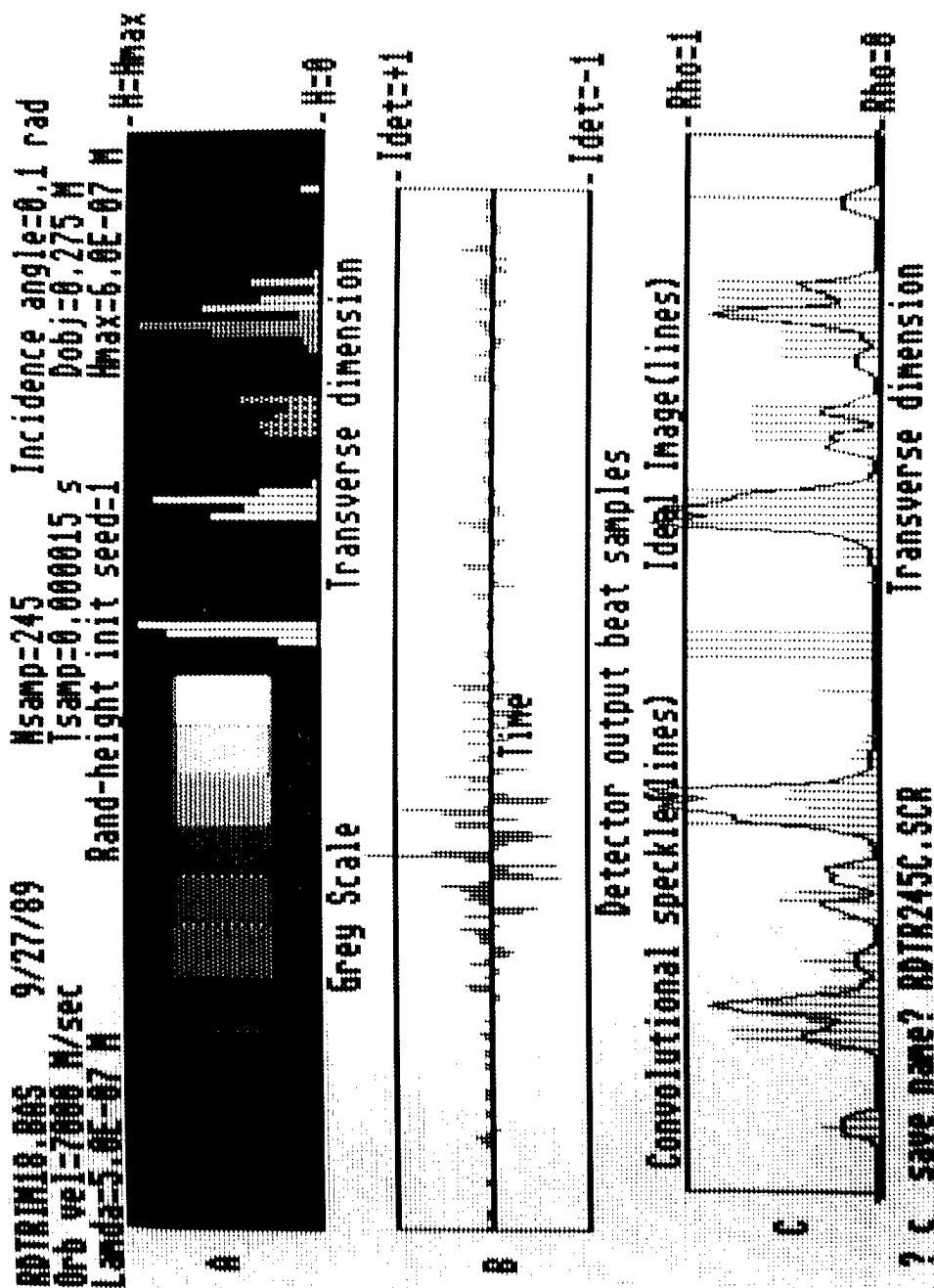
Figure 4-5. Doppler image with a three-scatter site extended reference. The extended reference both reduces resolution and increases speckling.

48
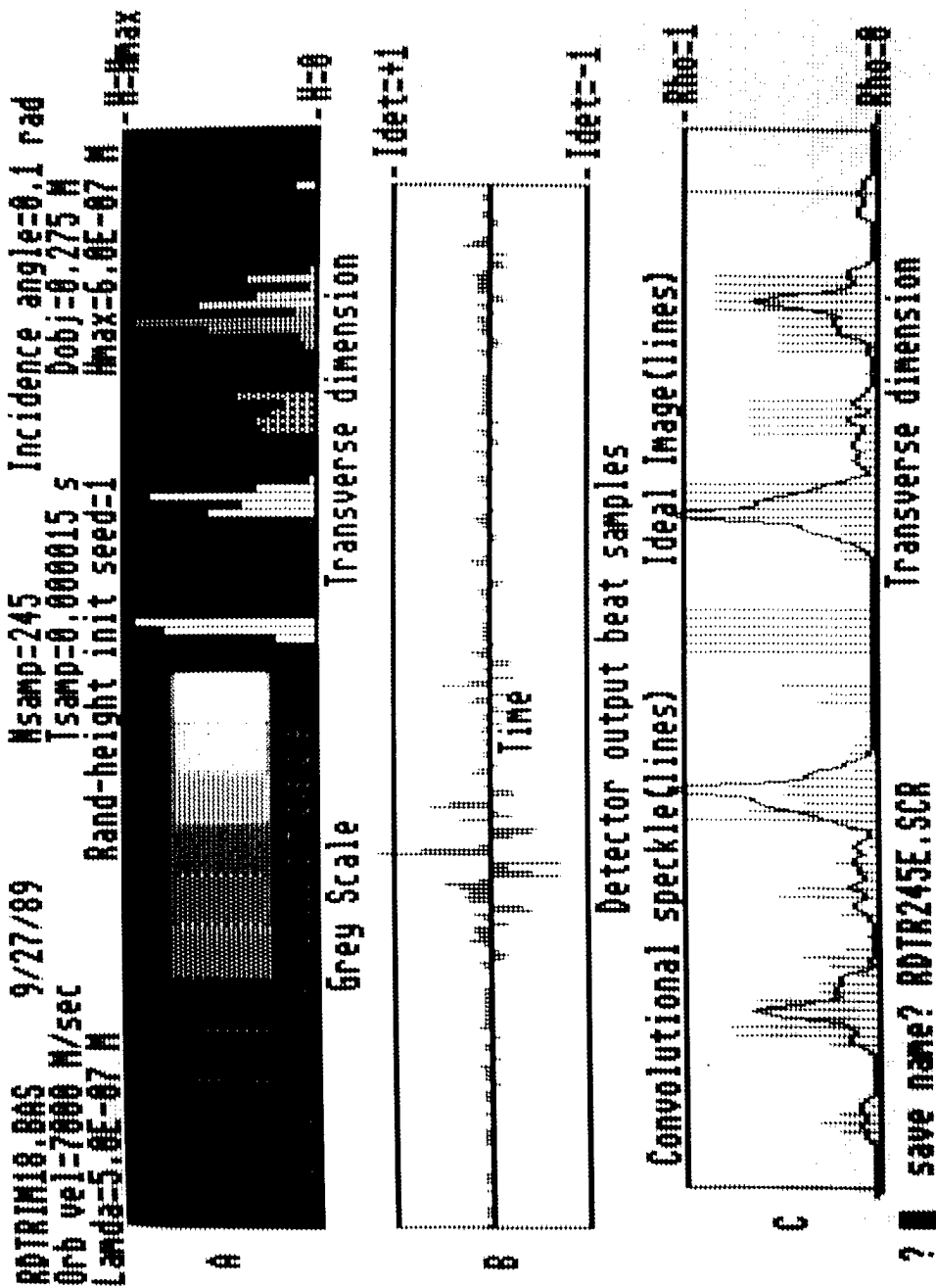
Figure 4–6.   Range-Doppler image with a five-scatter site extended reference.

4.3.1.2 Ranges. Each returning laser pulse is gated into time segments corresponding to the relative delays from different sections of the object.

4.3.1.3 OPD calculation. The Optical Path Difference (OPD) calculation is central to the accuracy of the amplitude and phase variations in the return wave. The largest and smallest dimensions in the calculation can be as much as 14 orders of magnitude apart, ranging between the orbital height (O), the radius of the object sphere (a), and the fraction of a wavelength that the object moves between laser pulses. The usual way to calculate OPD would have been to make small angle approximations and avoid incremental changes in the sin or cosine of a large number. However, since we were summing contributions over range depths much larger than a wavelength, we would still have had to keep an inordinately large number of decimal places in the calculation.

The solution we chose was to maintain separately, for each reflection point, both an initial OPD and coordinate location (x_s, y_s, z_s) on the sphere (Figure 4-7), and a changing ΔOPD and $(\Delta x_s, \Delta y_s, \Delta z_s)$ which accumulated with each rotation or movement of the object. The accuracy of the initial OPD was then not crucial; we expanded our OPD expression only to the level of the target dimensions, not to the wavelength. To track the target movement, we differentiated the OPD expression with respect to x,y and z coordinates, calculated dx,dy and dz for each movement, and integrated numerically to obtain the current coordinates of each reflector. Initialization of the OPD and the analytic expressions for its derivatives are given in Appendix A.

(a)

(b)

Figure 4-7.   (a) Axis directions and (b) coordinates and
dimensions, used in the RD-TRIMS sphere model.

4.3.1.4 Step size. The sampling time Δt is determined by the maximum estimated doppler shift. This was calculated as follows:

Translation $\quad \Delta f_t \sim 2v_t a/0\lambda$

Rotation $\quad\quad \Delta f_r \sim 2a\Omega/\lambda, \quad \Omega=\Omega_x, \Omega_y, \text{ or } \Omega_z$

Vibration $\quad\quad \Delta f_v \sim 2H_v\Omega_v/\lambda$

$$\Delta f_{max} \sim \Delta f_t + \Delta f_r + \Delta f_v$$

where V_t is translated velocity along x, Ω_x, Ω_y, and Ω_z are the angular velocities around the x, y and z axes, H_v is the vibrational amplitude, and $\Omega_v = 2\pi fr$, the vibrational frequency.

The beat frequency between the range and reference waves will be offset from DC by passing the reference beam through a modulator. We chose a modulation frequency $f_m=2\Delta f_{max}$ or $4\Delta f_{max}$ that was large enough to give clear isolation between the range-reference beats and the low-frequency self-mixture beats from each range. To center the modulation on the Fast-Fourier Transform spectrum, the full frequency range was typically set at $2f_m=8\Delta f_{max}$, requiring a sampling time $\Delta t=16\Delta f_{max}$.

4.3.1.5 Calculation sequence. The sequence of calculations in the RD-TRIMS sphere model are illustrated in Figure 4-8. The following calculational sequence was followed for each new laser pulse:

- time step
- update OPD and coordinates for each reflector
- sum field contributions from points within each range   bin.

$$U_J = \sum_N e^{ik[OPD]_{N,J}} \qquad\qquad U_{ref} = \sum_N e^{ik[OPD]_{N,ref}}$$

$$I_J = |U_J + U_{ref}e^{i\omega_m t}|^2$$

52

GLINT POSITIONS
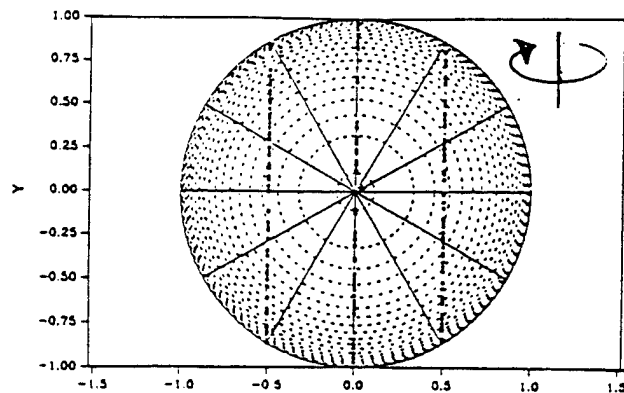
- *Point reflectors*
  - *random location along lines*
  - *random height 0. to 0.1 mm*
  - *uniform reflectivity*
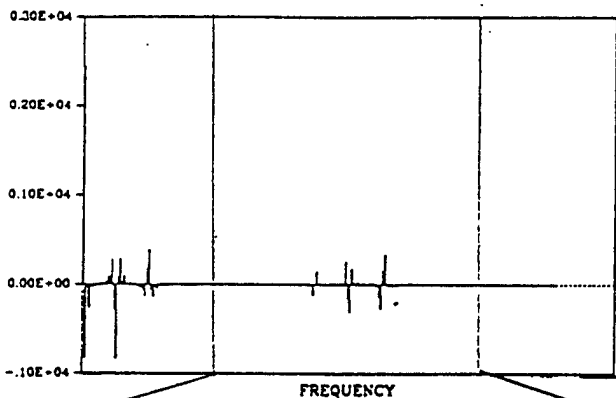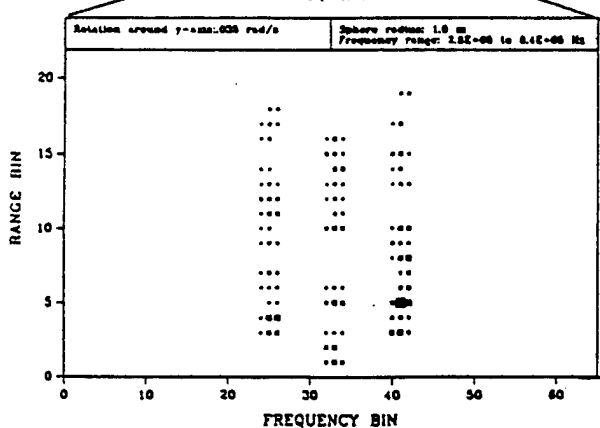- * *Reference reflector*
- ------ *Range boundaries*
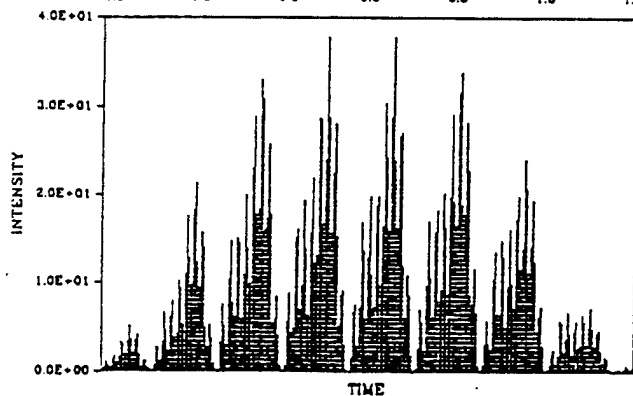
- *256 laser pulses*
- *rotate sphere between each shot*
- *add coherent return from each point*

$$U = \sum_{N} e^{ik[OPD]_N} \qquad U_{ref} = \sum_{N_{ref}} e^{ik[OPD]_{ref}}$$

$$I = |U + U_{ref} e^{i\omega_m t}|^2$$

ω_m: *reference modulation freq.*

SAMPLE TIME TRACE

- *Fast Fourier Transform*

SAMPLE FREQUENCY TRACE

- *Expand frequency range x2*
- *Average 2 points/frequency bin*
- *→ 64 bins*

RANGE–DOPPLER SIGNATURE

Figure 4-8.   Sequence of calculations for 3 reflecting bands on a rotating sphere.

53

where U_J and U_{ref} are proportional to the return fields at the receiver from the N points in the Jth range or reference range, ω_m is the offset frequency applied via a modulator to the reference wave, and I_J is proportional to the pulse intensity incident on the range bin detector.

Most of the sample calculations were made with the assumption that the gating of the return pulse would separate the ranges into unique bins. This would occur if the spatial pulse length was much shorter than the range depth. Towards the end of the program, an option was added to the code to reflect the mixing between adjacent ranges that would result from a pulse length equal to the range depth.

4.3.1.6 Signal processing.

A succession of 256 I_J's for each range bin formed the digitized time trace. At this point we introduced options such as pulse shaping, noise, and subtraction of the dc average. A frequency spectrum for each range bin was then obtained via a Fast Fourier Transform (FFT). A gaussian pulse shape was usually chosen so that the beginning and end of the pulse train would not trigger spurious responses in the FFT. In addition, the average value was subtracted out before transformation so that a large dc component would not cause a mis-scaling of the spectral display.

The frequency spectrum for each range typically showed two groupings of signals: near-dc signals due to self-interference between the reflection points within a range, and signals grouped around the modulation frequency ω_m due to the beating of the range wave against the reference wave. The latter is, of course, the desired signal, and the former will be filtered out. Our code accomplishes this by displaying only the center portion of the frequency spectrum. In addition, the display groups adjacent points in the digital spectrum together into 64 frequency bins.

4.3.2 RD Images of Rotating, Translating, and Vibrating Spheres.

This part of our study was aimed at demonstrating the type of patterns obtained in imaging lines or bands of reflectors on a rotating, translating, or vibrating sphere. We used the following parameters:

sphere radius (a): 1 m.
Orbit height (O): 2×10^5 m.
wavelength (λ): 0.5 μm

4.3.2.1 Rotation. Figure 4-9 shows the RD-TRIMS images formed by 1, 3, or 5 bands of reflectors encircling a rotating sphere. Approximately 200 reflection points were scattered randomly along the lines. From the direction of the laser source, these bands appear as straight lines on the surface.

When the rotation axis of the sphere is parallel to the direction of the lines, we obtain a reasonably accurate representation of the reflectors. The line images are broadened by the frequency resolution limits imposed by the length of the pulse train. Speckle-induced hot spots are also apparent, but they do not cause any significant loss of image information for our monotone images.

When the rotation axis is perpendicular to the lines, however, the image remaps into unfamiliar patterns and may appear as distorted. Image information is lost by a symmetry that causes the 3 lines to appear as 2 and the 5 lines as 3 (2 of which blur together). The parallel and perpendicular line cases probably represent the best and worst cases, respectively, of image ambiguity in our study.

4.3.2.2 Rotation/translation ambiguity. Figure 4-10 illustrates the ambiguity between the RD-TRIMS image of a rotating and translating sphere. For each reflecting point, the
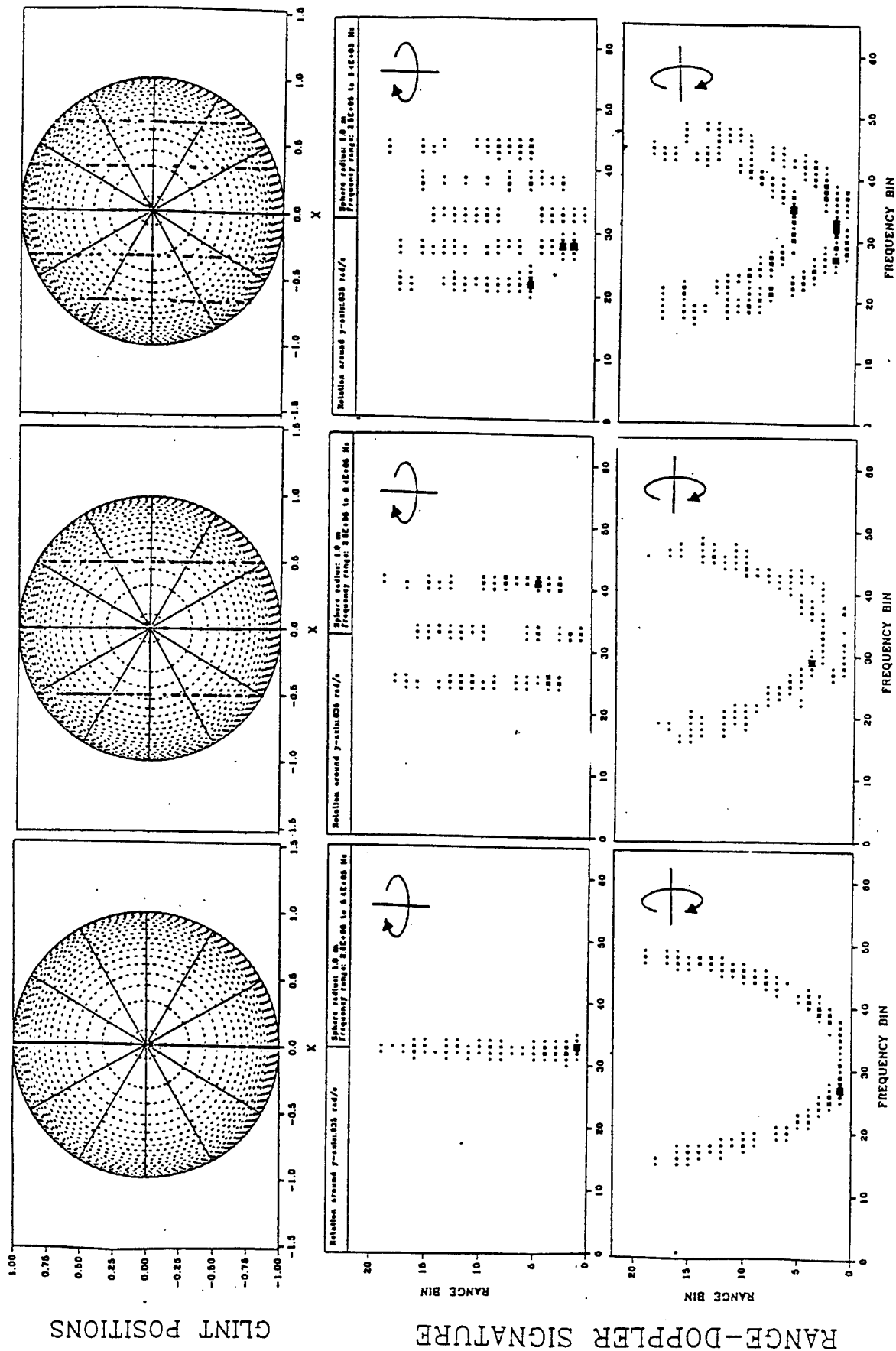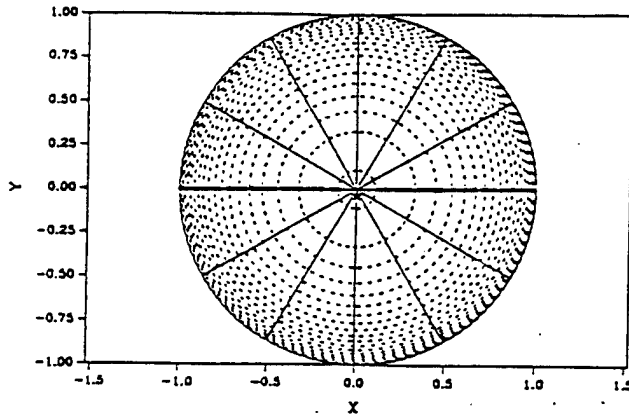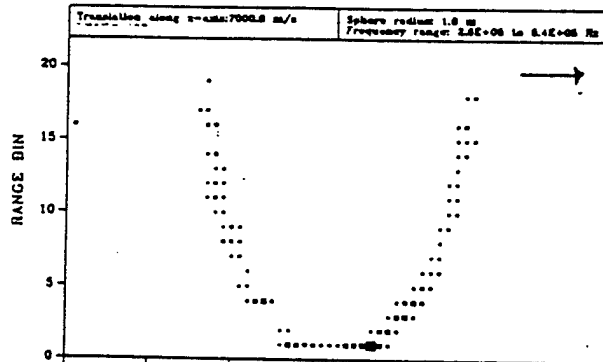
Figure 4-9.   RD-TRIMS images of 1, 3 or 5 bands of reflectors on a rotating sphere.

Signatures can only be distinguished with supplemental data.

- *Local reference whole-body doppler signature*
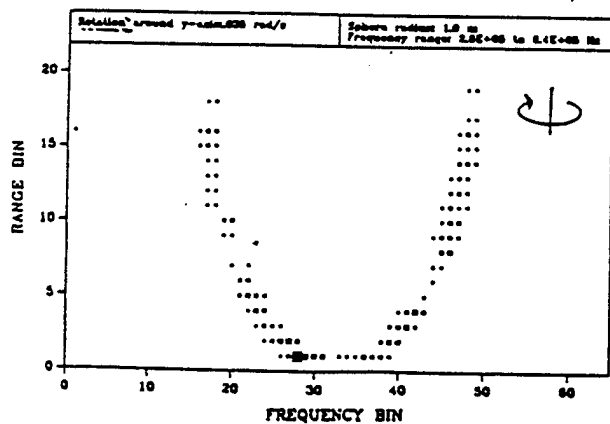- *Knowledge of probable orbit height or spin rate*

GLINT POSITIONS

RANGE–DOPPLER SIGNATURE

- *Translation*

- *Rotation*

Figure 4-10. Ambiguity in determining whether object is rotating or translating if no other motion information is available.

relative velocity component in the direction of the receiver is proportional to (a) its distance from the rotation axis or (b) from the axis perpendicular to the direction of translation. Thus a slow rotation (.035 rad/s) looks identical to a typical orbital translation (7000 m/s). Such signatures can be distinguished with supplemental data such as a whole-body doppler signature obtained with a local reference, angular track rates, or knowledge of probable velocities and spin rates.

4.3.2.3 Vibration and translation. A combination of translation and vibration patterns for a single line or band of reflectors are shown in Figure 4-11. The vibration pattern is the lowest order mode, in which the sphere's radius varies sinusoidally. We ran two cases with radial variation

$$a = 1. + H_v \sin(2\pi f_v t)$$

choosing first two vibration frequencies f_v=5 Hz and f_v=200 Hz, then juggling the vibration amplitude a_v and translation velocity v_t to obtain good display patterns. The requirements were (1) comparable doppler shifts for vibration and translation, and (2) one case with a fraction of a vibration cycle during the run and a second case with several vibration cycles during the run. The two cases shown in the figure are as follows:

	Case 1	Case 2
H_v (m)	$1. \times 10^{-3}$	$1. \times 10^{-7}$
f_v (Hz)	5	200
v_t (m/s)	7000	30
Δf_v (Hz)	1.3×10^5	5.0×10^2
Δff (Hz)	1.4×10^5	6.0×10^2
T_f (s)	1.2×10^{-4}	2.9×10^{-2}
$T_f f_v$ (cycles)	.0006	5.8

VIBRATION SIGNATURES

Figure 4-11. RD-TRIMS signatures of a single reflecting band on a sphere undergoing a combination of translation and vibration.

where $T_f = [8(\Delta\nu_v + \Delta\nu_t)]^{-1}$ was the temporal length of the 256-pulse run.

The RD-TRIMS image in case 1, where only a fraction of a vibration cycle is encompassed, shows a simple skewing of the pattern due to translation. This is due to the addition of the vibration and translation doppler velocities in the direction of the receiver. In case 2, with more than one vibration cycle during the run time, the result is an FM spectrum within each range bin, with mode spacing f_v.
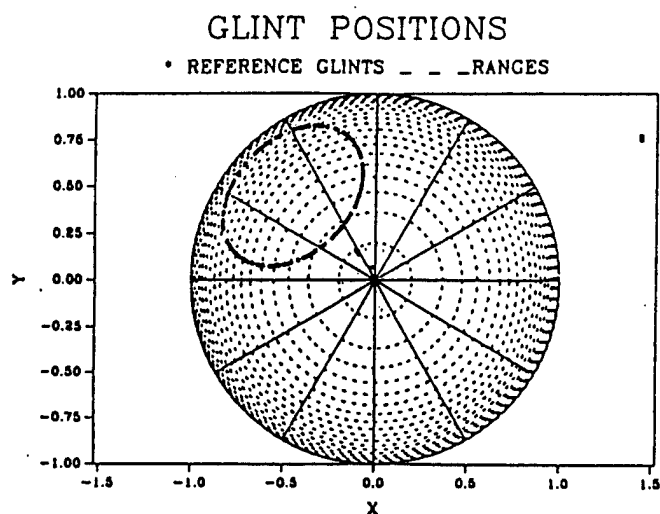
4.3.3 RD Image Degradation.

Image degradation can be a blurring or broadening of the image against a background, or an obscuration of the image by background noise. In this section we examine the results of simulations that include multiple or extended reference glints and noise from low light levels or detector dark currents.
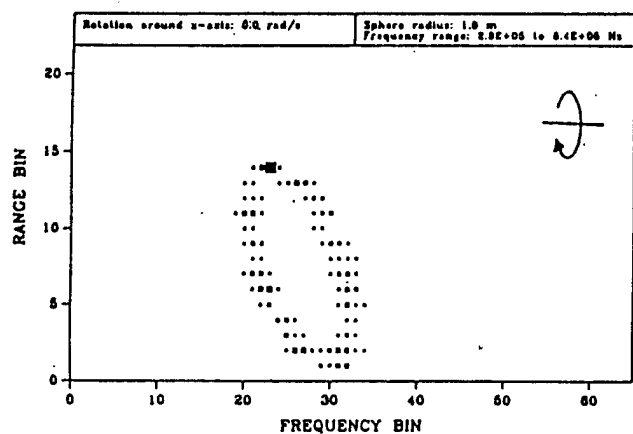
4.3.3.1 Single versus multiple reference glints. For this study our imaging object was an off-axis circle of 200 randomly spaced reflectors. The reference range included either one or ten glints. In Figure 4-12, it can clearly be seen that the image formed by the 10 glints is degraded by blurring.

4.3.3.2 Random background and extended reference glints. The result of the previous section does not specify whether image blurring occurs because of speckling effects between multiple glints or simply because multiple glints take up a larger area. We therefore looked at the effect of fixing the number of reflectors in the reference range, but making the reference range smaller.

We again used the off-axis circle of reflectors but included a random background that might obscure its RD-TRIMS image. The circle and random background were each composed of 100 equal-
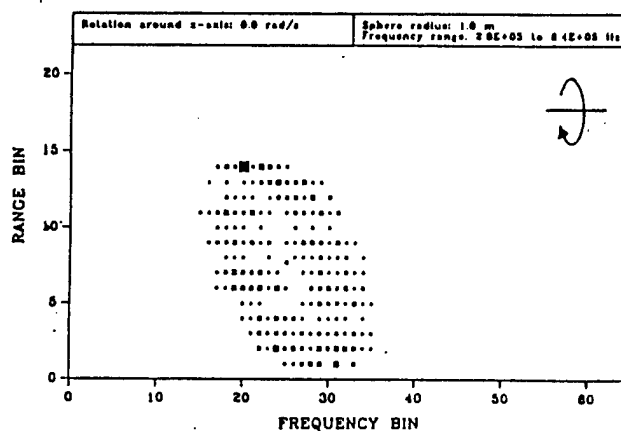
GLINT POSITIONS

* REFERENCE GLINTS _ _ _RANGES

GLINT POSITIONS

* REFERENCE GLINTS _ _ _RANGES

RANGE—DOPPLER SIGNATURE
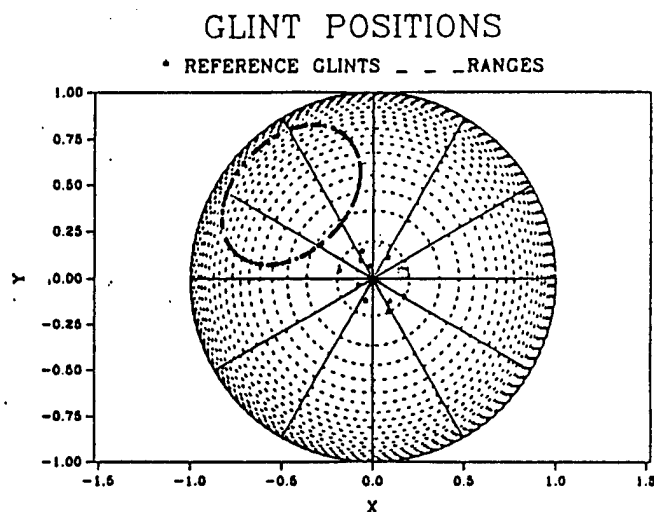
RANGE—DOPPLER SIGNATURE

* Image of an off-axis circle

* 10 reference glints

Figure 4-12.   Single versus multiple reference glints with an off-axis circle of reflections on a rotating sphere.

61

intensity reflectors. The reference range contained 10 more of these reflectors.

In Figure 4-13, the size of the reference range is varied to mimic the consequences of an extended reference glint. The result is an image that is broadened by convolution with the image of the reference glint. As the reference glint approaches the size of the object to be imaged, the image becomes unrecognizable. The multiplicity of the glints is not important as long as they are clustered close together. A simple conclusion is that the reference reflector needs to be smaller than the object to be resolved.

4.3.3.3 Noise at low light levels. Primary sources of noise in the system will be shot noise from low light levels and detector dark current. In the model, noise is handled by summing the average number of detector electrons generated by the light and by the dark current, and randomizing the actual electron count with a poisson statistic noise generator.

The average number $\langle N \rangle$ of electrons from one range bin detector per pulse is given by

$$\langle N \rangle = \left| \ U\sqrt{N_{ph}} \ + \ U_{ref} \ e^{i\omega t} \ \sqrt{\frac{N_{ref}}{N_r}} \ \right|^2 \eta E \ + \ N_{el}$$

where U = field from image reflectors

U_{ref} = field from reference reflectors

N_{ph} = average number of photons per pulse per reflector (except for the reference reflectors)

N_{ref} = average number of photons per pulse per reference reflector

N_r = number of ranges

η = detector quantum efficiency

E = pulse envelope (typically Gaussian in time)

N_{el} = average number of dark current electrons per pulse.
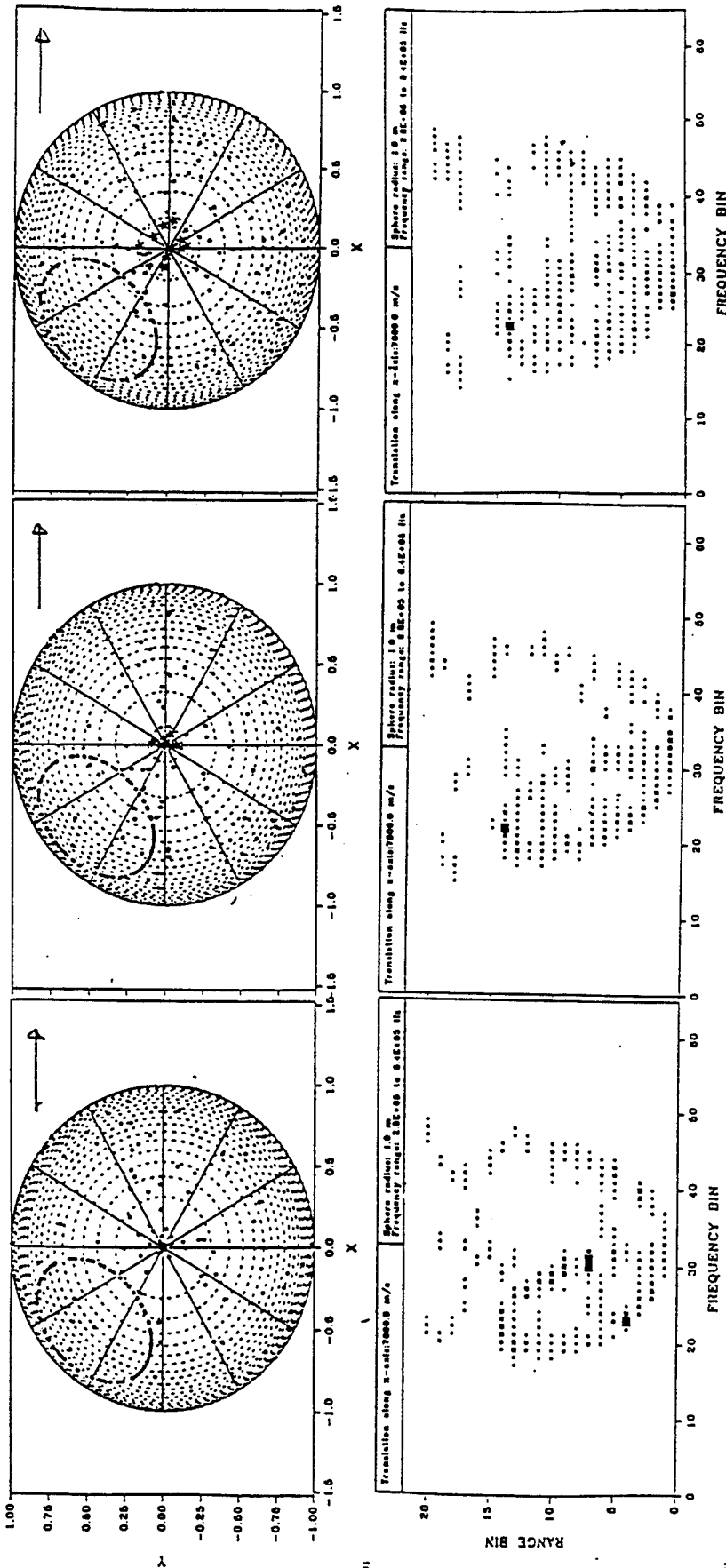
Figure 4-13. Imaging an off-axis circle of reflectors against background of random reflectors; translating sphere.

63

The poisson noise generator takes the sequence of expectation values $\langle N \rangle$ and generates a sequence of actual electron counts with the correct statistics. One asks the following question: What is the probability P that there are fewer than K_e electrons generated? For poisson statistics, the answer is

$$P = e^{-\langle N \rangle} \sum_{K=0}^{K_e} \frac{\langle N \rangle^K}{K!}$$

The noise generator turns this question around; it selects a random probability between 0 and 1, then defines the randomized number of electrons to be the nearest (on the large side) K_e that gives this probability.

The three variables that we adjusted during this study were N_{ph}, N_{ref}, and N_{el}. In Figure 4-14, we again used the off-axis circle as the imaging object on the surface of the sphere. These runs show the effect of varying the return signal photons and the detector dark current. Over the two decades of variation shown, we span the range from a nearly noise-free image to one that is completely obscured. For this set of runs, the returns from the reference reflectors were 20 times the strength of the returns from the range reflectors. This meant that the reference reflector signals, after being split among our 20 range bins, would be of equal effective strength as the range reflectors.

In Figure 4-15, we fixed the detector dark current at 10 electrons/pulse, chose either 20 or 200 photons per range reflector (N_{ph}) and varied N_{ref} between 20 and 2000. In these runs, the sphere had just 5 randomly placed reflectors rather than an identifiable object pattern. Over two decades of variation in N_{ref}, the images of the 5 points were transformed from total obscuration to recognizable images.
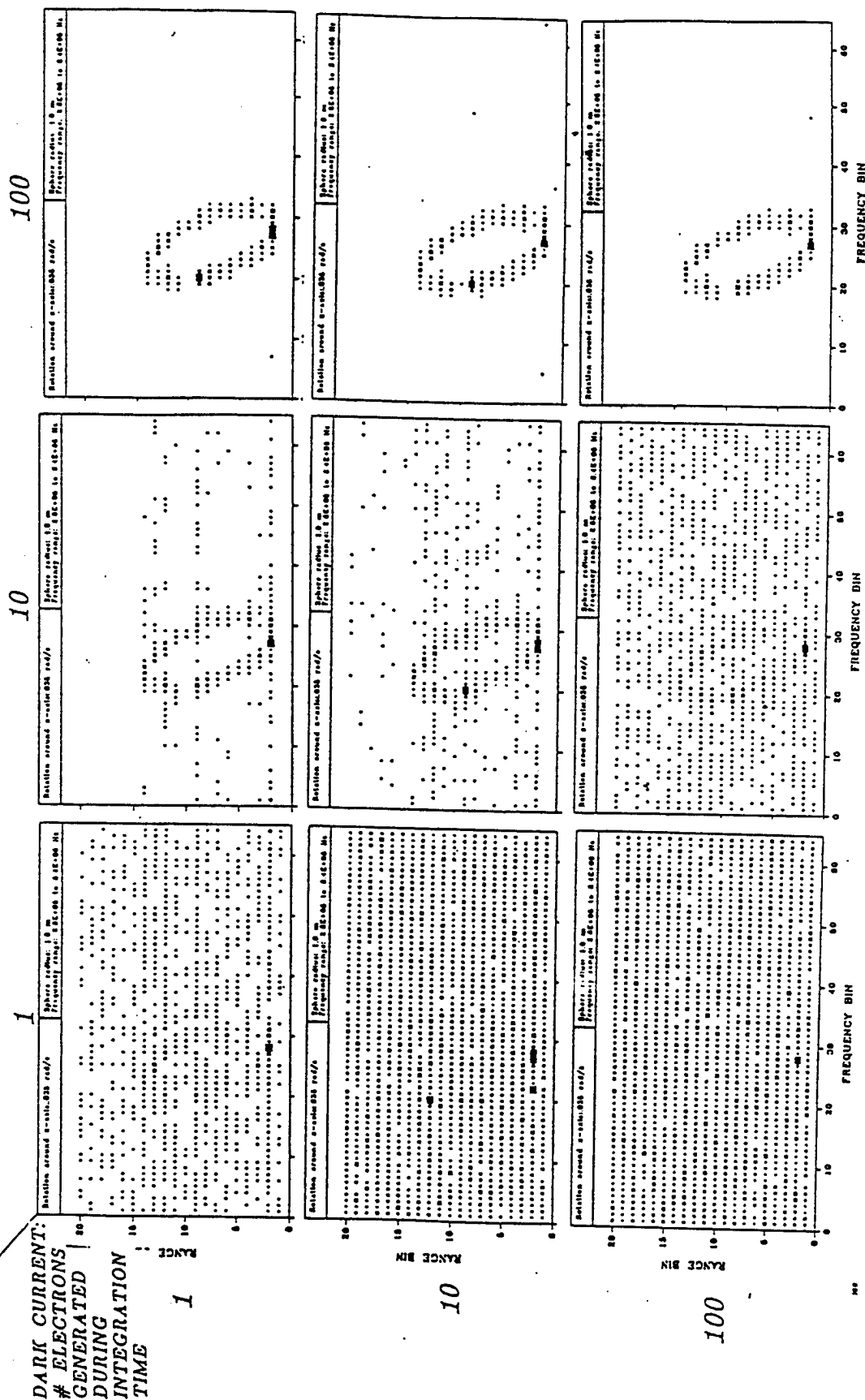
Figure 4-14. Noise at low light levels.

65

GLINT POSITIONS
• REFERENCE GLINTS — — —RANGES

#PHOTONS/
REFERENCE
GLINT

• *Quantum efficiency 0.2*
• *10 dark current electrons/pulse*
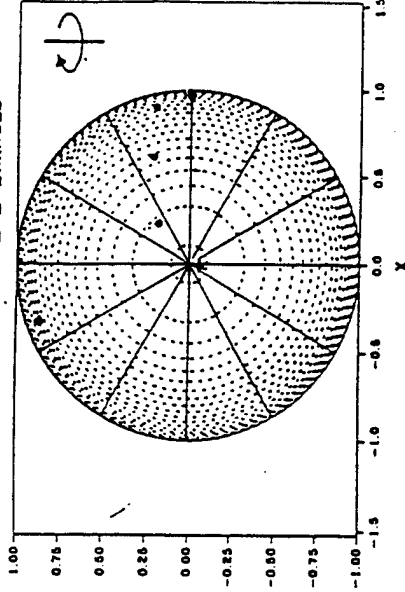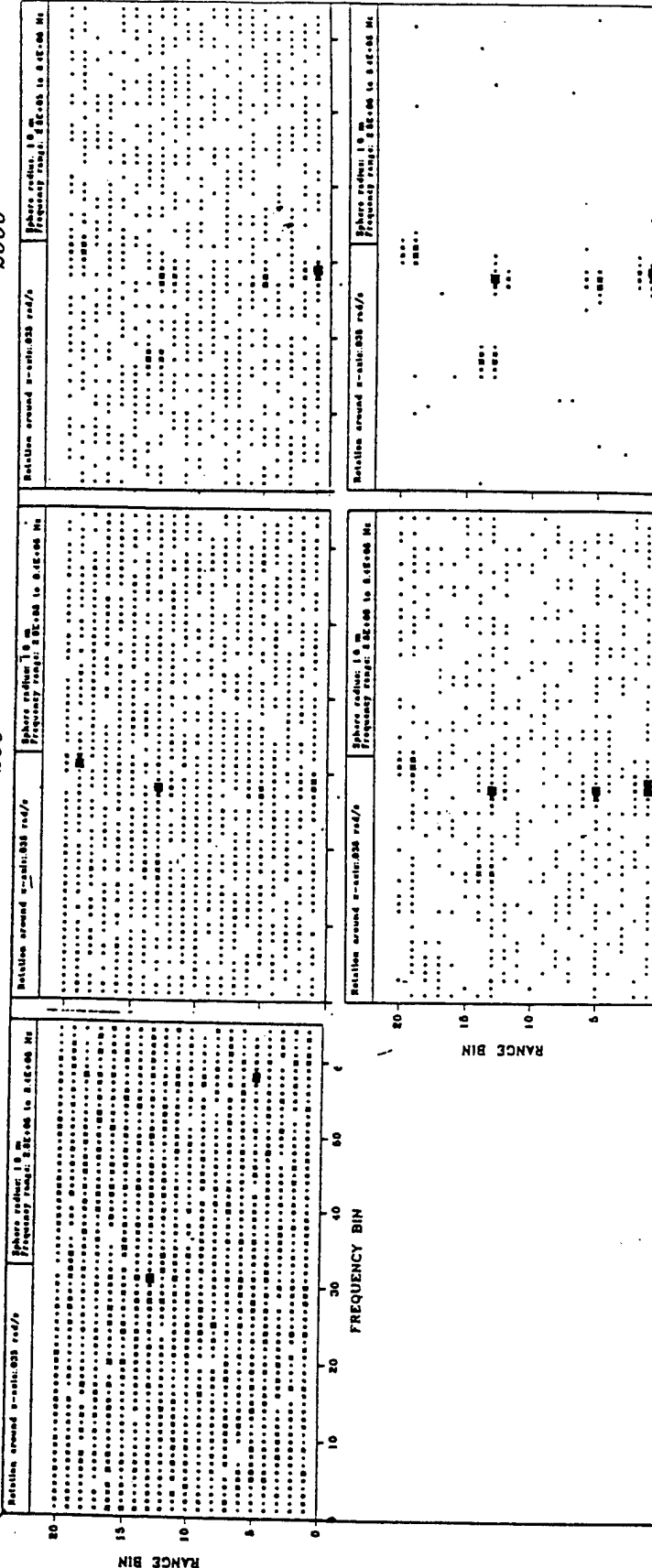
PHOTONS/
IMAGE GLINT

Figure 4-15. Effect of reference reflectors noise at low light
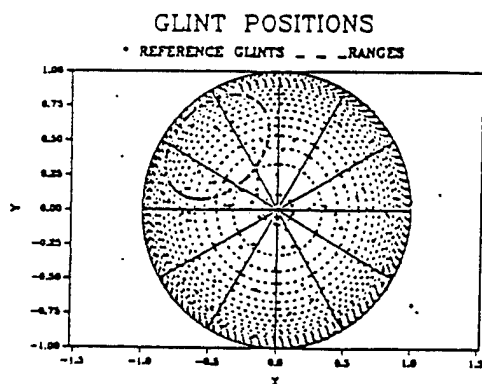levels; 5 randomly positioned image reflector as
shown.

4.3.4 Comparison with Other Techniques.

We used the code to compare the imaging ability of RD-TRIMS with that of other doppler imaging techniques. These runs only addressed imaging ability and not practicality or signal-to-noise. In Figure 4-16, the imaging object is again taken to be the off-axis circle with the random scatter reflector background.
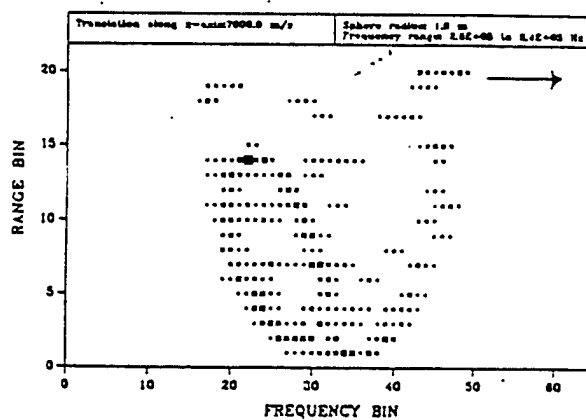
4.3.4.1 Local reference. We first looked at a system referenced by a local oscillator. A rotating object gives the same image whether the system is self-referenced or local-oscillator referenced. (Note that the image reversal of the rotating sphere is simple due to the opposing direction of movement of the reflecting surface.) In translation, however, the local oscillator system must track the movement of the object to avoid a blurring-out of the image. This auxiliary system is avoided in RD-TRIMS.

4.3.4.2 Autodyne. Autodyne is a system of whole-body self-referencing. It does not appear to give any detailed imaging information.
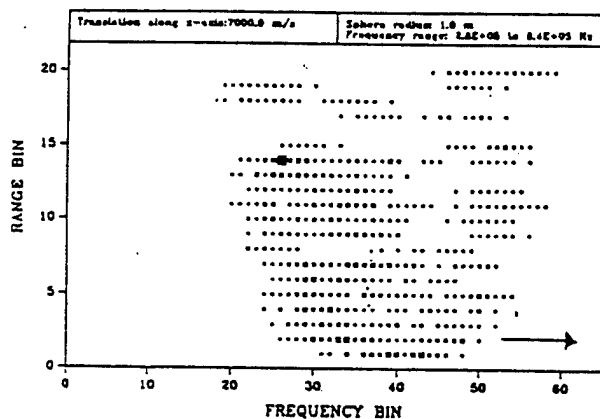
The last run in the figure is one where we tried self-referencing within each range, but keeping the ranges separated. We thought that this might yield more information than autodyne, but it again seems difficult to extract the desired image.
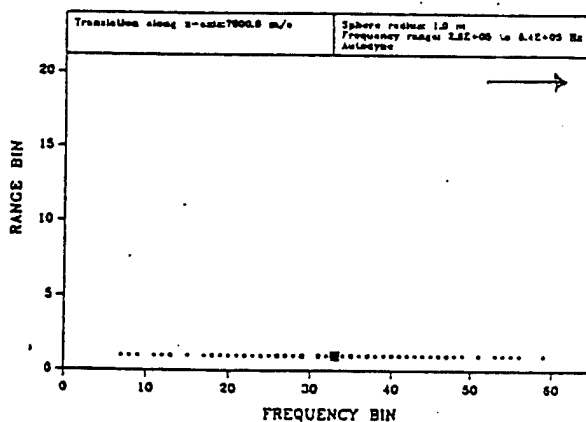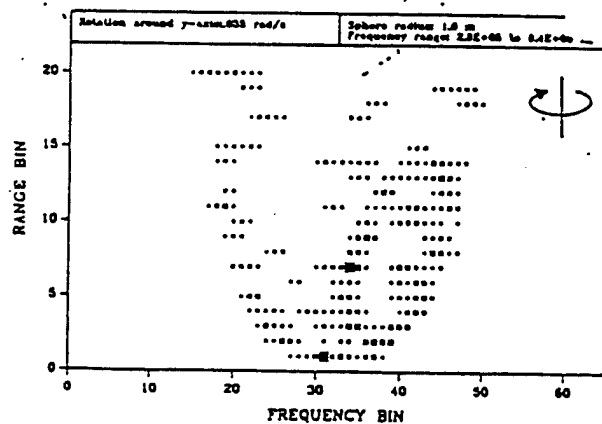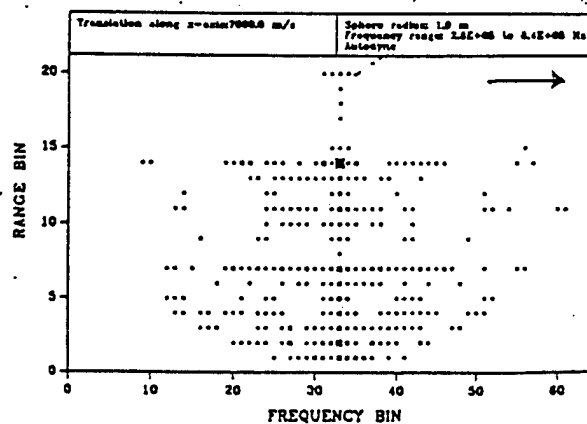
Figure 4-16. Comparison of RD-TRIMS with other referencing techniques.

68

SECTION 5

CONCLUSIONS

5.1 FLAT PLATE MODELING RESULTS

We found that the changing aspect ratio of the RD-TRIMS imaging process produced good speckle reduction and superior images, compared to single-shot (single-wavelength) angle-angle images. It should be noted that the speckle averaging is a consequence of the basic range-Doppler imaging process and not specifically of the self referencing. In particular, operating with extended references appears to reduce the effectiveness of the averaging process. We also processed a number of our target model returns by beating the entire target against itself (Autodyne) and, in contrast to the RD-TRIMS images, found little image information in the extended spectrum which this produced. We could not find any way of recovering the basic image information from this Autodyne spectrum.

5.2 SPHERE MODELING RESULTS

We investigated the RD-TRIMS imaging of simple surface patterns in the form of circles and stripes and found that,with ideal references, either accurate images or "signature" images were produced. For example depending on pattern orientations, with respect to the rotation axis, stripe "images" are sometimes rendered as true images and sometimes remapped into other shapes. Our results indicate that these remappings often produce a unique signature, but sometimes an ambiguous image results. In comparison, we note that (in the three-dimensional sense) angle-angle images may also be highly ambiguous. However, we did not explore these ambiguity questions in any depth, since any such comparisons will be strongly object dependent.

Our reference reflectors were all located within the first range gate, which selected scatter sites on the leading edge of

the sphere. The number and lateral extent of the scattering elements was variable. When the lateral extent encompassed the entire range bin we observed a smearing of the resulting RD-TRIMS images, as expected. However, our test patterns were still discernible.

At low light levels, we examined the quality of images obtained with varying combinations of detected photons and dark current electrons. For example, with an image glint reflecting 20 photons, a reference glint reflecting 200 photons divided among 20 ranges, a detector quantum efficiency of 20% and 10 dark current electrons per detector per pulse, the image was just barely discernible above the noise. With ten times more photons, the noise background was almost gone.

5.3 S/N ANALYSIS RESULTS

We investigated S/N performance both by computer simulation and classical analysis. Our analytical results compared the S/N performance of the self-referencing (RD-TRIMS) system against an ideal, quantum-limited RD system. The analysis assumed that the shot noise generated by the returns from the total image scatter sites, encompassed within one range bin, overrides any (non-target) background or dark current noise. We find that the relative S/N is degraded with increasing number of RD resolution cells and decreasing reference strength. In the limit of very high brightness references, the system approaches ideal quantum limited performance. Although not all references will be bright enough to generate quantum limited S/N, there are S/N enhancement factors when comparing to a 10.6 μm RD system. If the 10.6 μm RD system operates with the same illuminator power we typically gain by a factor of R^2 [R is the wavelength ratio 10.6/$\lambda(\mu$m)], because of the tighter illumination beam, and lose by a factor R, because of the higher energy per photon at the shorter wavelengths. Thus, we gain by a factor of R , independent of S/N considerations.

It is hard to directly compare the S/N of RD-TRIMS to that of Autodyne, but we conclude that the average S/N in an Autodyne Doppler bin is identical to that in one RD-TRIMS range and Doppler bin, at the same wavelength.

APPENDIX A
OPD Calculations for the Sphere

The Optical Path Difference (OPD) calculation is central to the accuracy of the amplitude and phase variations in the return wave. The largest and smallest dimensions in the calculation can be as much as 14 orders of magnitude apart, ranging between the orbital height (O), the radius of the object sphere (a), and the fraction of a wavelength that the object moves between laser pulses. The usual way to calculate OPD would have been to make small angle approximations and avoid incremental changes in the sin or cosine of a large number. However, since we were summing contributions over range depths much larger than a wavelength, we would still have had to keep an inordinately large number of decimal places in the calculation.

The solution we chose was to maintain separately, for each reflection point, both an initial OPD and coordinate location (x_s, y_s, z_s) on the sphere, and a changing ΔOPD and $(\Delta x_s, \Delta y_s, \Delta z_s)$ which accumulated with each rotation or movement of the object. The accuracy of the initial OPD was then not crucial; we expanded our OPD expression only to the level of the target dimensions, not to the wavelength. To track the target movement, we differentiated the OPD expression with respect to x, y and z coordinates, calculated dx, dy and dz for each movement, and integrated numerically to obtain the current coordinates of each reflector.

Calculation of the initial OPD is based on the coordinates shown in Figures A-1a and 1b. We have 3 sets of coordinates for each reflection point. The points themselves are at x_p, y_p and z_p. Each sits a distance H above the coordinates x_s, y_s and z_s which lie on a perfect sphere of radius a. OPD is calculated in the direction of the laser source; we set up a reference sphere of radius O, with points x_r, y_r and z_r at the intersection of the
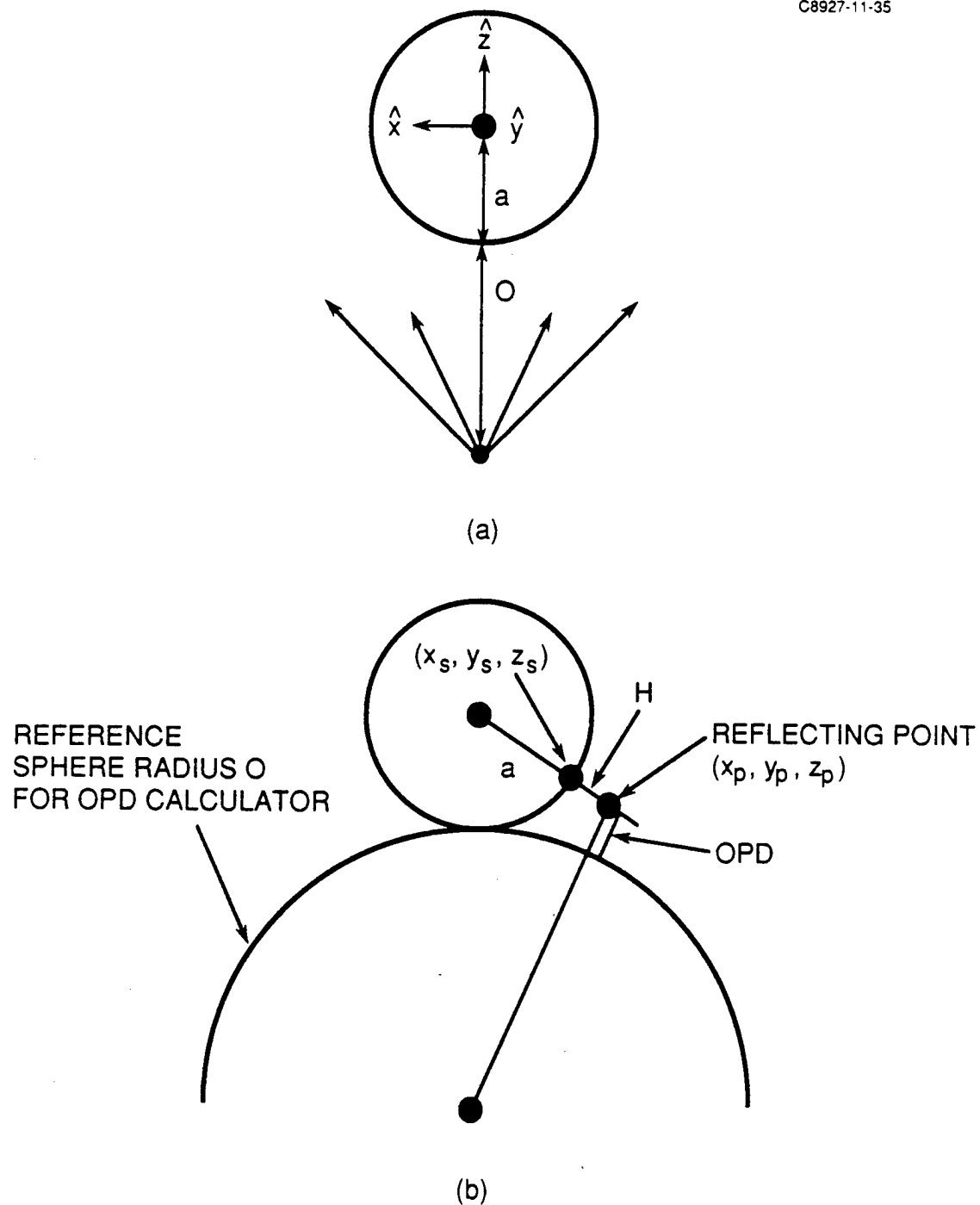
C8927-11-35

(a)

(b)

Figure A-1. (a) Axis directions and (b) coordinates and
dimensions, used in the RD-TRIMS sphere model.

73

reference sphere and the line connecting the reflecting point and the laser source. Combining the x's and y's into single transverse coordinates $b=(x^2+y^2)^{1/2}$, the geometrical relationships are

$$b_s^2 + z_s^2 = a^2$$

$$b_r^2 + (0+a-z_r)^2 = 0^2$$

$$b_p = b_s(1 + H/a)$$

$$z_p = z_s(1 + H/a)$$

$$\frac{(0+a-z_r)}{(0+a-z_p)} = \frac{b_r}{b_p}$$

$$OPD = 2 \left[(b_p-b_r)^2 + (z_p-z_r)^2\right]^{1/2}$$

Folding the relationships together and manipulating yields

$$OPD = 2 \left[(0+a-z_p)^2 + b_p^2\right]^{1/2} - 0$$

or, approximately

$$OPD \simeq 2 \left(a - z_p + \frac{B_p^2/2}{(0+a-z_p)}\right)$$

The code contains, not the OPD expression itself, but its differentials with respect to the possible directions of motion: $\partial(OPD)/\partial x_s$, $\partial(OPD)/\partial y_s$, $\partial(OPD)/\partial z_s$, and $\partial(OPD)/\partial H$. At each time step we accumulate the OPD and coordinate differentials:

$$x=x_s+\Delta x_s \qquad \Delta x_s=\Delta x_s^*+dx$$
$$y=y_s+\Delta y_s \qquad \Delta y_s=\Delta y_s^*+dy$$
$$z=z_s+\Delta z_s \qquad \Delta z_s=\Delta z_s^*+dz$$

$$OPD = (OPD)_{initial} + \Delta OPD$$

$$\Delta OPD = \Delta OPD^* + \frac{\partial (OPD)}{\partial x_s} dx + \frac{\partial (OPD)}{\partial y_s} dy + \frac{\partial (OPD)}{\partial z_s} dz + \frac{\partial (OPD)}{\partial H} dH$$

where * represents the quantities accumulated in previous time steps. Coordinate steps depend on the type of movement; for example

Translation in x: $\quad dx = v_t \Delta t$

Rotation around y: $\quad dx = x \cdot [\cos(\Omega_y \Delta t) - 1] + z \cdot \sin(\Omega_y \Delta t)$

$$dz = z \cdot [\cos(\Omega_y \Delta t) - 1] - x \cdot \sin(\Omega_y \Delta t)$$

$$dy = 0.$$

Vibration $\quad dH = H_v \Omega_v \Delta t \cdot \cos(\Omega_v \Delta t)$

where v_t is the translational velocity along x, ω_y is an angular velocity around the y axis, H_v is the vibrational amplitude, ω_v the vibrational frequency, and Δt the sampling time between laser pulses. To obtain an adequate sampling rate the coordinate steps must be fractions of a wavelength. Thus $\omega_y \Delta t \ll 1$ is required, and both $[\cos(\omega_y \Delta t) - 1]$ and $\sin(\omega_y \Delta t)$ must be expressed as a small-angle series to avoid calculational roundoff errors.